Optical Diagnostics in Energy Conversion Processes

Bi, Ruike

2024

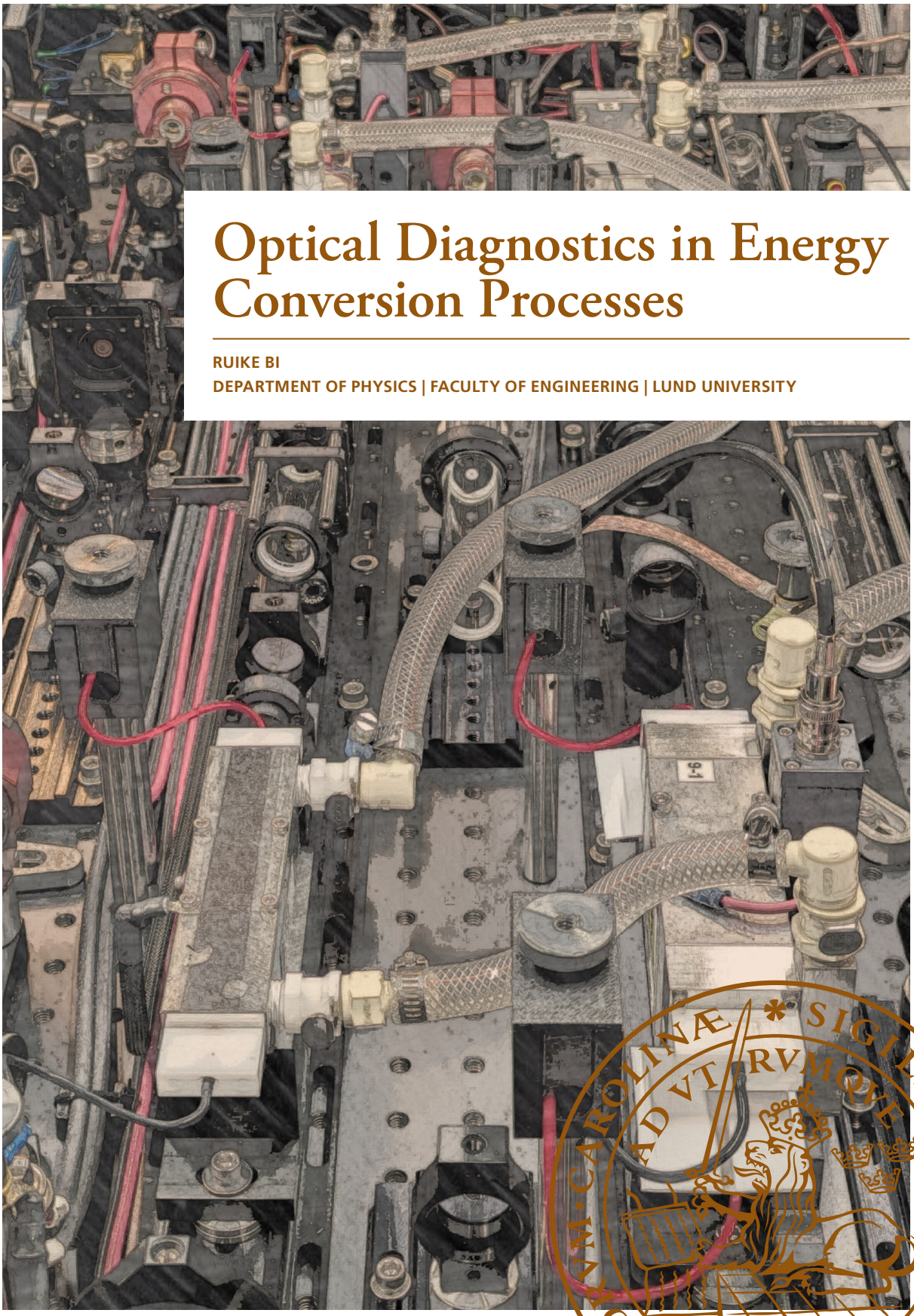

Optical Diagnostics in Energy Conversion Processes

RUIKE BI
DEPARTMENT OF PHYSICS | FACULTY OF ENGINEERING | LUND UNIVERSITY

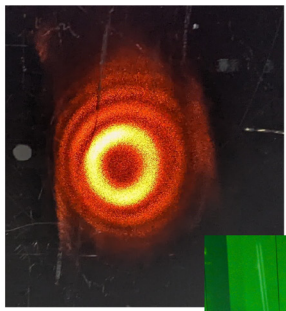

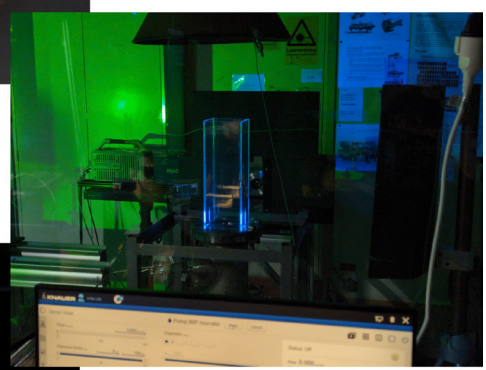

Printed by Media-Tryck, Lund 2024 NORDIC SWAN ECOLABEL 3041 0903

LUND UNIVERSITY

Faculty of Engineering
Department of Physics

ISBN 978-91-8104-117-0
ISSN 1102-8718
ISRN LUTFD2/TFCP-256-SE

Optical Diagnostics in Energy Conversion Processes

Optical Diagnostics in Energy Conversion Processes

Ruike Bi

LUND UNIVERSITY

DOCTORAL DISSERTATION

Doctoral dissertation for the degree of Doctor of Philosophy (PhD) at the Faculty of Engineering at Lund University to be publicly defended on 27th of September at 09:15 in the Rydberg Hall, Department of Physics, Professorsgatan 1, Lund

Faculty opponent
Mikhail Slipchenko

Organization: LUND UNIVERSITY

Document name:DOCTRAL DISERTATION **Date of issue:** 2024-09-27

Author(s): Ruike Bi **Sponsoring organization:**

Title and subtitle: Optical Diagnostics in Energy Conversion Processes

Abstract:

This thesis presents development in optical diagnostics for studies of energy conversion processes. Work has been done in characterization of electrode wear in spark plugs, multi-species high-speed tomographic laser-induced fluorescence, high-speed diagnostics in lab-scale gas turbine burners, and surface temperature measurements on gas turbine burner injection nozzles.

A new method of monitoring erosion of the electrodes in spark plugs made from nickel has been established, based on the emission of Ni atoms in the 339~360 nm spectral range. Spectral study revealed the spectral range in which high intensity of Ni atomic emission can be observed while low intensity of background emission is present. An excitation scan has shown that laser excitation at Ni's 336.957 nm absorption line can induce the most optimum signal-to-noise ratio in the desired detection window. The fluorescence lifetime of the found excitation scheme has been measured, reporting an effective fluorescence lifetime of approximately 1.1 ns, which was not seen to be changing as the spark discharge plasma decays. It has been further established that the integrated fluorescence intensity of the current excitation scheme is proportional to the Ni atom number density. Such findings have created a solid foundation for further 2D studies on the generation of Ni atoms from the spark discharge and erosion of the electrodes.

The construction of an injection seeded OPO producing signal wavelength at 609 nm pumped by a high-speed burst mode laser system has been described. A routine of alignment of the OPO cavity has been established and described in detail in the thesis. Using the same laser system, quasi-simultaneous 10 kHz tomographic LIF measurement of anisole and formaldehyde has been successfully performed, where only two sets of high-speed CMOS and image intensifier were used for acquisition of 8 views from different angles thanks to the application of an improved sensor splitting strategy. The eight acquired views were successfully placed on the same horizontal plane also due to the improved strategy. A novel imaging timing design succeeded in the quasi-simultaneous acquisition of fluorescence signal from two species on the same imaging sensor.

High-speed formaldehyde planar laser-induced fluorescence measurements have shown insufficient droplet breakup and evaporation in a Triple Annular Research Swirler burner using ethanol as fuel. High amount of ethanol droplets has been observed in the LIF sequences. In addition, it has been shown that excess formaldehyde was trapped in the outer recirculation zone. The averaged flow structure in the outer recirculation zone has been demonstrated by optical flow estimation performed on the acquired formaldehyde LIF sequence.

Finally, a study on the injection nozzle surface temperature of a lab-scaled gas turbine burner has been presented. A galvo system was used for automated temperature measurement on a 2D array of points on the burner surface. It was found that the surface temperature of the injection nozzle was affected by the cooling from the supplied fresh gas and heating from the flame. Specifically, increased heating could be observed when a flame attached to the injection nozzle.

Key words: Laser Diagnostics; Combuston Diagnostics; High-speed; Imaging: Laser-induced Fluoresence; Fluorescene Lifetime; Burst-mode Laser;

Classification system and/or index terms (if any) **Supplementary bibliographical information**

Language: English **ISSN and key title**: 1102-8718

ISBN: 978-91-8104-117-0 (print) and 978-91-8104-118-7 (electronic)

Recipient's notes: **Number of pages:** 98

Price: **Security classification:**

Signature Date 2024-08-19

Optical Diagnostics in Energy Conversion Processes

Ruike Bi

LUND UNIVERSITY

Front cover illustration: Picture of the optical setup of Quasi-modo, taken by Ruike Bi.

Back cover illustration: (Top to bottom) beam profile of the OPO's 609 nm output; TARS burner during laser measurement; a methane jet flame with a flat pilot, taken by Ruike Bi.

Funding information: The PhD position was financially supported by KAUST (OSR-2018), Swedish Engergy Agency (50180-1, 44120-1) and European Research Council (852394)

Faculty of Engineering

Department of Physics

ISBN: 978-91-8104-117-0 (print)

ISBN: 978-91-8104-118-7 (electronic)

LRCP: LRCP-256

ISSN: 1102-8718

ISRN: LUTFD2/TFCP-256-SE

Printed in Sweden by Media-Tryck, Lund University

Lund 2024

Media-Tryck is a Nordic Swan Ecolabel certified provider of printed material. Read more about our environmental work at www.mediatryck.lu.se

MADE IN SWEDEN

To mom and dad,

thank you for all the love and support.

悔相道之不察兮，延伫乎吾将反。
回朕车以复路兮，及行迷之未远。

步余马于兰皋兮，驰椒丘且焉止息。
进不入以离尤兮，退将复修吾初服。

路漫漫其修远兮，吾将上下而求索。

Table of Contents

Abstract

This thesis presents development in optical diagnostics for studies of energy conversion processes. Work has been done in characterization of electrode wear in spark plugs, multi-species high-speed tomographic laser-induced fluorescence, high-speed diagnostics in lab-scale gas turbine burners, and surface temperature measurements on gas turbine burner injection nozzles.

A new method of monitoring erosion of the electrodes in spark plugs made from nickel has been established, based on the emission of Ni atoms in the 339~360 nm spectral range. Spectral study revealed the spectral range in which high intensity of Ni atomic emission can be observed while low intensity of background emission is present. An excitation scan has shown that laser excitation at Ni's 336.957 nm absorption line can induce the most optimum signal-to-noise ratio in the desired detection window. The fluorescence lifetime of the found excitation scheme has been measured, reporting an effective fluorescence lifetime of approximately 1.1 ns, which was not seen to be changing as the spark discharge plasma decays. It has been further established that the integrated fluorescence intensity of the current excitation scheme is proportional to the Ni atom number density. Such findings have created a solid foundation for further 2D studies on the generation of Ni atoms from the spark discharge and erosion of the electrodes.

The construction of an injection seeded OPO producing signal wavelength at 609 nm pumped by a high-speed burst mode laser system has been described. A routine of alignment of the OPO cavity has been established and described in detail in the thesis. Using the same laser system, quasi-simultaneous 10 kHz tomographic LIF measurement of anisole and formaldehyde has been successfully performed, where only two sets of high-speed CMOS and image intensifier were used for acquisition of 8 views from different angles thanks to the application of an improved sensor splitting strategy. The eight acquired views were successfully placed on the same horizontal plane also due to the improved strategy. A novel imaging timing design succeeded in the quasi-simultaneous acquisition of fluorescence signal from two species on the same imaging sensor.

High-speed formaldehyde planar laser-induced fluorescence measurements have shown insufficient droplet breakup and evaporation in a Triple Annular Research Swirler burner using ethanol as fuel. High amount of ethanol droplets has been observed in the LIF sequences. In addition, it has been shown that excess formaldehyde was trapped in the outer recirculation zone. The averaged flow structure in the outer recirculation zone has been demonstrated by optical flow estimation performed on the acquired formaldehyde LIF sequence.

Finally, a study on the injection nozzle surface temperature of a lab-scaled gas turbine burner has been presented. A galvo system was used for automated temperature measurement on a 2D array of points on the burner surface. It was found

that the surface temperature of the injection nozzle was affected by the cooling from the supplied fresh gas and heating from the flame. Specifically, increased heating could be observed when a flame attached to the injection nozzle.

Popular science summary

Studies have shown that the use of fire by our ancestors is evident as early as a million years ago. Since then, combustion has provided humans with cooked food, warmth, light, and safety. As we advance into modern society, combustion of fossil fuels such as coal, oil, and natural gas has been the major source of energy for industries and our daily life. Despite being such an important role to the human civilization, the large-scale fossil fuel combustion in today's world has brought serious environmental challenges, for example air pollution of nitrogen oxides and particle matters, and global warming from the excessive emission of CO2.

Having realized the harm to the earth brought about by traditional fossil fuel combustion, the world is now working hard to amend what has been done. Many scenarios have been proposed for our world to reach a balance between the emission and capture of CO2 in the near future, i.e. the net zero emission goal. This, however, doesn't mean that research into combustion should be terminated. Although electrification is the star of a carbon-neutral future, combustion still will be a big contributor with the majority of the fuel switched to renewables, as predicted by the International Energy Agency, and continued research into combustion to boost the efficiency and reduce pollutant generation is vital to achieving this goal.

You may want to ask here, why optical diagnostics? Why must there be lasers and seemingly unnecessarily complicated mirrors and lenses? Well, combustion in the real world is a lot more complicated than the simple oxidation reaction we learned in high school textbooks. Even for methane, which is the simplest hydrocarbon fuel, hundreds of intermediate reactions can happen, giving rise to more than 50 different kinds of molecules and radicals present in the flame. This is where the first advantage of optical diagnostic comes in: the ability of distinguishing different molecular species. Different molecules and radicals emit light signals that are of specific wavelengths, or colour, of light when excited. So, by detecting the spectrum emitted by a flame, we can have an idea of what species are in it. And even better, they also absorb light differently. Therefore, by sending a beam of light that is intense and single-color, i.e. a laser, of the right wavelength into a flame, certain species that are of interest to us can be selectively made to emit light and thereby being detected.

To add to the complexity of combustion study, it is more than just the chemistry that affects the reactions. Many physical aspects of a flame are also vital to the understanding of the combustion. For example, knowing the temperature of a flame can tell us important basic characteristics of it, and temperature of the surrounding of a flame can be vital for engineering purposes. The flow field of the flame is also important, as it affects how the fuel is mixing with the air and affects how the areas are distributed where chemical reactions are happening. While conventional detection methods using physical probes can give information on these to a certain

degree, the presence of the probes would disturb the original field, therefore distorting the measurement results. This is called an intrusive approach. Optical diagnostics, on the other hand, have the strong advantage that they are not intrusive, thereby giving more accurate results of the original field.

In the work of this thesis, many optical diagnostic techniques have been used to study various processes centred around combustion. A major part of the thesis work was the construction of an optical parametric oscillator, which can convert the wavelength of the incident laser to longer wavelengths. Using state-of-the art laser systems, various laser-induced fluorescence measurements were carried out on spark plug discharges as well as propane flame in a Bunsen burner, yielding information about erosion of the spark plug electrodes and 3D distribution of formaldehyde and fuel in a turbulent flame. Remote measurements of surface temperature were also performed on a down-sized gas turbine burner, providing information of local heating on the nozzle induced by pure methane and hydrogen-enriched methane. The work of this thesis helps industry in designing better spark plug ignition strategies and provides novel ideas for improving existing optical diagnostic techniques.

Acknowledgements

Now my journey as a PhD student is about to come to an end. After spending all these years in this loving division, it is almost surreal that the time has actually come for me. So now I shall try my best to express my gratitude for the people I met during this epic journey.

Mattias, what an amazing supervisor you have been! As a supervisor, you not only guided us with your knowledge and experience in research, but also inspired with your humorous, optimistic personality. And you drive go-kart so well! I have a feeling that I may be the student who burned the most things in the lab, but that never stopped me from trying because every time I came to you with burned optics, you were only nice and supportive, telling me not to worry. I have also had moments of doubt. And whenever I talk to you about it, you were always able to cheer me up and give me the energy needed for keep going. For that I am so deeply grateful.

More than just the most amazing supervisor, I am also lucky enough to be working with the most amazing research group. I will for sure miss the group meetings where we discuss papers and have so much fun. Panagiota, it was so great working with you! Thank you for guiding me with working with the laser. Thank you for keeping the order in the lab. Thank you for being there for me when I'm in need. We will for sure carry the friendship to the many more years to come! David, it was such pleasant to work with you. Thank you so much for helping make the tomography measurement possible. In addition, it was such pleasure to share my enthusiasm in nerdy stuff with you. Kailun, together we have done some great stuff! I'd like to thank you for both help with the work and with life. And I wish you all the best in your years to come. Henrik, I am most impressed by the way you are able to organize your work. I learned a great deal when we worked together. And I want to thank you for your advice on my writing. Alexios, it was just great to have you as a friend and a colleague. I've enjoyed so much every single conversation we had. And special thanks to you for your remote lectures on Schlieren when I was in Ghent. Saeed, you were always so nice and gentle, yet so passionate and about the things you like. Glad I could get you into F1, and your effort in making me interested in football was all failure. A seed has been planted. Megha, although you don't admit it, I count you as one of my fellow nerds. Imagine my surprise when I found out that you know so much about Japanese and even Chinese anime and series. Now that you are going to inherit the Quasi-modo, hopefully you can find this book useful. Sebastian, you are a talented researcher and an honest advisor. Your feedback sessions were priceless and very much appreciated. Aravind, I feel that we kind share the same mentality as we are both quite troubled by the hardware. Things will get better, so good luck with both work and life! Jan-peter, although we haven't met for very long, I've enjoyed your company in the lab and on the lunch table. I will always remember "fear and hunger". To the fresh members of the group, Pranjal and Weilun, welcome to the best group there is! You'll have some great fun here.

Apart from members of the Mattias group, I was also fortunate enough to have worked with some other brilliant minds. Bora, thank you for the work together with the TARS burner, and thank you for many nice lunch talks. David A., although FRAME unfortunately didn't work out eventually, it was pretty cool to have you demonstrating the technique. Francesco, we had some fun time running the CECOST burner, and I wish you all the best at work.

Arman, we've been officemate for many years. It was so nice that I could talk to you when I wasn't clear of things as a fresh PhD student. It was also so nice to always have your warm greetings every day I came to work. I'm very happy for you that you are now advancing your academic career at the Aviation School and wish you all the best. Lovisa, you are such a nice and warm person. And it was a lot of fun hearing about what you do studying aerosol. We shared a happy moment when you published your first paper as first author, and that was precious. My first paper actually came slightly later when you are parental leave, preparing to welcome a new life into the world. I hope that you can have all the happiness.

Marcus, Per-Erik, and Joakim, I want to thank you for creating and maintaining this great division. The division really feels much more than just a workplace, but rather a big family. This is not possible without your hard work. Minna, Cecilia, Emelie, Igor and Josefine, thank you very much for taking care of all out needs, big and small, and keeping the division working smoothly. We would never have such a nice working environment if it weren't for you. Andreas, thank you for your valuable input on my manuscripts, and for your uplifting spirit. Sven-Inge, I've been not very punctual about my ISPs, thank you for putting up with it and helping me work it out. Edouard, your talent in Chinese is impressive! I'd also like to thank you for bringing so much fun to the division. Christian, thank you so much for always kindly answering my questions about everything.

My fellow colleagues, present and past, thank you very much for being part of this great family. Yupan, what a nice friend, and what a nice teammate you are! That is both in research and in Dota. Zhiyong, David F, Niklas, Edouard, David S., the bike trips were epic! We must keep it going. Saga, Adrian, Haisol, Dina, Pengji, Joakim J., Maria, climbing was a lot of fun! Thank you for introducing me to such a great sport. Jinguo, you are already a mature researcher. I wish you great success in your career. Adrian, Arman, Joakim J., Qiu Yue, Lisa, Christofer, the badminton sessions were a lot of fun, and I miss it. Can, congratulations on getting married and on your success on the Humboldt Scholarship! Xin and Qingshuang, thank you for being such nice friends. Martin, Jonas, Vassily, Manu, Elin, Karolina, Sebastian F., thank you for bringing up so much to the lunchroom! The discussions over lunch were golden. Xianzhong, Zhaomin, Qianjin, it was so nice having you as visitors and so nice that we got share a lot of fun times together. Mikkel, Armand, Simon, Johan F., Göran, Sabrina, Jefry, Alexander, Elias, Cuong, Meng, Zhongshan, Hampus, Elna, Frederik, Meena, Pontus, Frej, Anna-Lena, Birgitta, August, Johan Z., Alsu, Wubin,

Chengdong, Ali, Marco, Shen, Sandra, you all have my deep gratitude. Thank you for making the division such a great place.

Thanks also goes to friends I met outside of the division. Zhao Yue, thank you and I wish you all the best for the future. Dr. Zhang Yuhe, congratulations on making it! Miaoxin, what a PhD journey you have had! I hope that you have a smooth ride to the goal. Huaiyu, thank you for your wonderful cooking! Yingzhe and Bofei, it's about time we get the team together and have some fun! Shuo, how amazing life is that we become neighbours again so many years after our masters. Jinzhuo, thank you for being my first roommate in my PhD. Good luck to you at work!

I want to thank also some old friends. Members of the Wuhan University Astronomy Association, Song Yanran, Gao Chengkuan, Li Chen, Xu Qiuyang, Wang Zihan, Zhao Wenhua, Chen Xi, Zhao Yuxiao, Qiu Xiaoyu, Wang Chen, Zhou Xuan, Wu Haixu, Chen Ruiming, I was so lucky to be amongst you guys. The group chat was so much fun, though we usually talk about everything but astronomy. Li Zhenbo, we've known each other for many many years. Thank you for having all the weird discussions with me on including but not limited to math, algorithm, education, philosophy, Pokemon, and so much more. Lyu Shengyuan, congratulations on becoming a dad! And thank you for a lot of talks over life confusions, plus the guided tour to Huaqiangbei.

To my loving family, I can't thank you enough. Mom and Dad, you have planted the first seed of science in me when I was little. You have set the perfect role model, which led me to achieving this PhD. And most importantly, you have raised me under your wings with so much love. I don' t say this nearly enough, I love you so much!

Jundie, what a lucky guy I am to have met you! You are a great colleague. You work with such rigorous and devoted attitude. I get to learn a lot from you in our daily scientific discussions. Beyond that, you are such a wonderful partner. You have brought so many good things to my life with your passion for life, your love for nature, and your wills to act. I love you with the whole of my heart.

List of Papers

Paper I

Zhang, K., **Bi, R.**, Tidholm, J., Ängeby, J., Richter M., Ehn, A., **Detection of Nickel Atoms Released from Electrodes in Spark Discharges using Laser-induced Fluorescence**, manuscript accepted by *Appl. Spectrosc*.

Paper *II*

Bi, R., Zhang, K., Ehn, A., Richter, M., **Lifetime of Ni Laser Induced Fluorescence During Spark Plug Discharge**, *Appl. Phys. B* **130**, 147 (2024).

Paper III

Bi, R., Sanned, D., Stamatoglou, P., Richter, M., **Quasi-simultaneous, High-speed Tomographic Fluorescence Imaging of Fuel Tracer and Formaldehyde in a Propane Flame**, *submitted manuscript*

Paper IV

Feuk, H.; Pignatelli, F.; Subash, A.; **Bi, R.**; Szász, R.-Z.; Bai, X.-S.; Lörstad, D.; Richter, M. **Impact of Methane and Hydrogen-Enriched Methane Pilot Injection on the Surface Temperature of a Scaled-Down Burner Nozzle Measured Using Phosphor Thermometry**. *Int. J. Turbomach. Propuls. Power* 2022, 7, 29.

Related work

Paper A

Ängeby, J., Johnsson, A., Richter, M., **Bi, R.**, **SI Engines for Alternative Fuels - Combustion Phase and the Trade-off Between Ignitability and Spark Plug Wear**, *16th Int. MTZ Conference Heavy-Duty Engines*, November 10-11, 2020.

Abbreviations

AOM	acoustic optical modulator
ASE	amplified spontaneous emission
AWG	arbitrary waveform generator
BBO	beta barium borate
CW	continuous wave
EOM	elctro-optic modulator
FHG	fourth harmonic generator
FWHM	full width at half maximum
HGU	harmonic generation unit
ICCD	intensified charge-coupled device
ICE	internal combustion engine
ICMOS	intensified complementary metal-oxide semiconductor
LBO	lithium triborate
LIF	laser-induced fluorescence
OPO	optical parametric oscillator
PLIF	planar laser-induced fluorescence
PMT	photo-multiplier tube
QC	Quantum Composer
SHG	second harmonic generator
SNR	signal-to-noise ratio
TARS	Triple Annular Research Swirler
THG	third harmonic generator
UVFS	UV fused silica

1 Introduction

Historically, fossil fuels such as coal, oil and natural gas have been providing more than 80% of the energy needed by the human society since the industrial revolutions. Combustion, being the most widely used approach of energy extraction, has been used in many different sectors in the modern world, including but not limited to electricity generation, road, water and air transportation, heating, and industrial production [1]. The wide use of combustion of fossil fuels, however, brings about problems as well. One of the main products of fossil fuel combustion is carbon dioxide, which is a greenhouse gas that is responsible for raising earth's annual average temperature by about 1.1 ˚C over the past century [2].

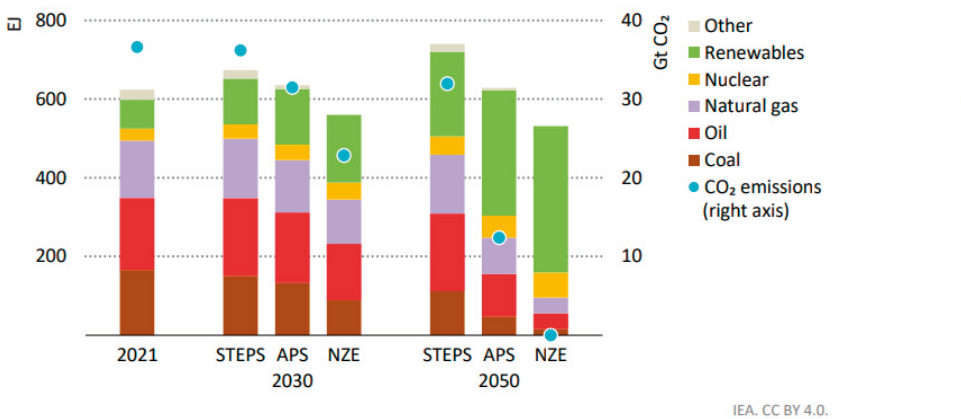

Figure 1.1: Total energy supplied by fuel and CO_2 emission projection by scenario. STEPS: the Stated Policies scenario; APS: the Announced Pledges Scenario; NZE: the Net Zero Emission by 2050 scenario [3]. © IEA

Looking into the future, the reduction of use of combustion and fossil fuels is a sure trend. However, this does not mean that research towards combustion should be terminated. In the projections suggested by the International Energy Agency (IEA) based on scenarios, more than 500 exajoules of energy will still be supplied by fuels

by the year 2050 in the Net Zero Emission by 2050 scenario [4]. It is also emphasized in IEA's World Energy Outlook reports that improvement on efficiency in existing infrastructure is a vital way of CO_2 emission reduction [3]. These statements strongly support that research on understanding combustion and pushing for cleaner, more efficient combustion plays an important role in the future of reaching a net zero CO_2 emission society.

Combustion is a process of great complexity in both chemistry and physics and research in combustion is a complicated topic covering multiple scientific disciplines. Combustion of a carbon based fuel can generate up to thousands of different intermediate species, and the involved reactions are controlled by both the chemical properties of the species and the transportation that is governed by physical laws [5-8]. High temperature and intense light emission generated by the combustion reactions creates a hostile environment which increases the difficulty of probing the process. Moreover, real-life combustion applications such as internal combustion engine (ICE) and gas turbines are turbulent processes. The turbulent nature adds a further challenge in fluid dynamics. All of these factors push us for applying advanced diagnostic approaches to better understand combustion, and therefore be able to improve its efficiency.

Optical diagnostics have unique advantages and have been proven to be a powerful tool in the field of combustion research. The non-intrusiveness of optical diagnostics ensures that the thermodynamic property and flow structures of the flame remain undisturbed. The introduction of laser-based techniques opens new possibilities in combustion research. Laser's narrow bandwidth enables species-specific diagnostics; it's high intensity significantly increases signal-to-noise ratio (SNR) and extends the detection limit to the ppm level; the short pulse width and narrow beam waist leads to sub-nanosecond temporal certainty and micrometre level of spatial certainty. In the past years, a lot of research has been conducted here at Lund University, proving the power of laser-based techniques [9]. Recent development of laser systems has seen the birth of a powerful burst mode laser system, Quasi-modo. Compared to traditional systems, the burst mode laser system can deliver high pulse energy (>100 mJ @1064 nm) at ultra-high repetition rates (>100 kHz) [10-14]. Such a powerful tool brings many possibilities in temporally resolved diagnostic on high-speed combustion events such as internal combustion engines and gas turbine burners.

The work of this thesis focuses on development of novel laser-based diagnostics in combustion related processes, using both traditional low repetition rate systems and the burst mode laser system. In chapter 2, a brief introduction covers some important concepts that help the readers understand the essence of this thesis. Following the introduction to basic theories, chapter 3 focuses on instrumentation. In this chapter, the structure and working principles of a state-of-the-art burst-mode laser system and a customized injection seeded optical parametric oscillator (OPO) will be described. Also included in this chapter are routines and experiences from the author

on the operation of the system. Chapters 4-6 will focus on presenting measurements performed on various applications centred around energy conversion processes, as listed below.

- Chapter 4: development of a diagnostic approach on electrode erosion and measurement of Ni atom fluorescence lifetime in a plasma environment.
- Chapter 6: high-speed formaldehyde PLIF and optical flow measurements in a gas turbine flame.
- Chapter 5: improvement on a view-splitting strategy and gating design to achieve successful quasi-simultaneous tomographic reconstruction of laser-induced fluorescence (LIF) from two species using only two high-speed cameras.
- Chapter 6: use of a galvo system to perform phosphor thermometry on a 2D matrix of detection points on the injection nozzles of a gas-turbine burner.

Finally, conclusions and outlook are made in chapter 8.

2 Background Theory

A wide variety of different optical diagnostic approaches have been used as a part of this thesis. In this chapter, the background theory to important fundamental concepts are provided to facilitate a smoother understanding of the main topics of the thesis.

2.1 Laser-induced fluorescence

LIF refers to the process where absorbance of the incident laser photons excites the molecule or atom to be studied to a higher energy level, and light is emitted when the molecule or atom de-excites back to lower levels. A schematic drawing of the process is depicted in Figure 2.1 [15]. Because molecules have fine splitting of energy levels due to vibration and rotation, a molecular LIF spectrum usually contains a band structure, as is illustrated in Figure 2.1 (a). In comparison, the energy levels of atoms are distributed sparser, resulting in a LIF spectrum of multiple sharp individual spectral lines, as is shown schematically in Figure 2.1 (b).

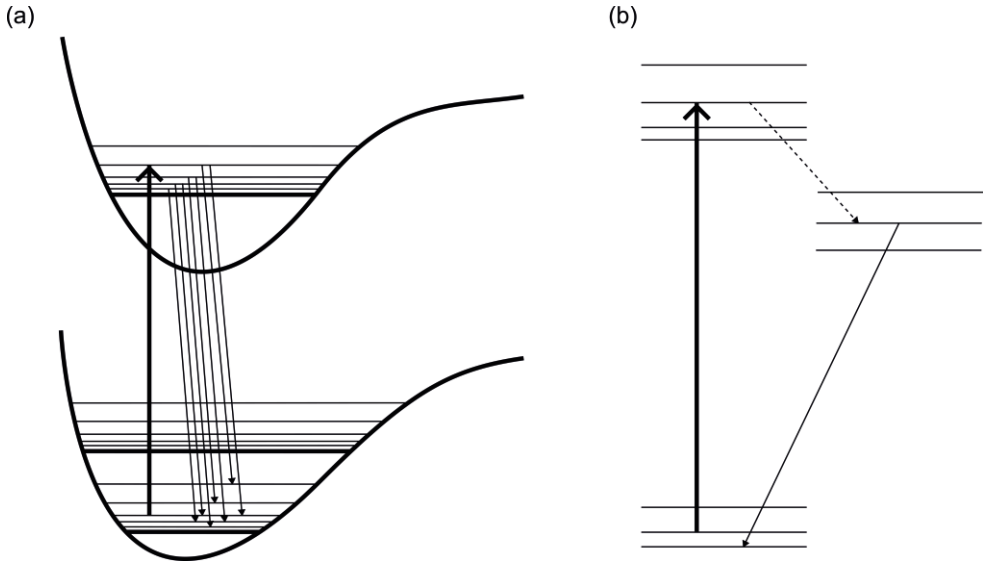

Figure 2.1: Schematic drawing of LIF in molecules (a) and in atoms (b). Thick arrows pointing up represent the excitation; solid arrows pointing down the emissions, and dashed line pointing down the non-radiative relaxation.

LIF is a powerful tool due to its non-intrusive, high SNR, species specific characteristics [16-19]. Various forms of diagnostics can be performed with LIF, including spectroscopic measurements [20-23], lifetime measurements [24-26], 2D measurements (planar laser-induced fluorescence, PLIF) [27-30], and even 3D measurements [31-35]. Versatile kinds of information can be gained in for example temperature, concentration field, flow characteristics, etc from LIF. Used in this thesis are LIF of three species, whose excitation and detection wavelengths as listed in Table 2-1.

Table 2-1: Excitation and detection wavelengths of species whose LIF emissions were studied in this thesis.

Species	Excitation wavelength (nm)	Detection wavelength (nm)
Anisole	266	~300-340
Formaldehyde	355	~370-570
Ni	336.94	~338-350

2.2 Second-order non-linear optics basics

As described in Chapter 2.1, laser at a specific wavelength is required for performing LIF on a species. However, laser systems based on a certain kind of gain media are usually restricted to one output wavelength. Second-order non-linear optical effects offer a powerful tool to perform laser wavelength conversion, granting us access to a much wider spectrum of light.

2.2.1 Origin of second-order non-linear optics

When a weak light wave interacts with a medium, typically a polarization density P that is linear to the weak incoming electric field $\mathcal{E}$ is introduced. This linearity, however, does not hold true if the electric field becomes as strong as about 10^5~10^7 V/m, which is comparable to the interatomic electric fields. Under such circumstances, non-linearity in the polarization density may appear, and subsequently, an expression between P and $\mathcal{E}$ can be written as follows, assuming that the high-order polarization densities are not significant [36]:

$$\begin{aligned} P &= a_1\mathcal{E} + \frac{1}{2}a_2\mathcal{E}^2 + \frac{1}{6}a_3\mathcal{E}^3 + \cdots \\ &= \epsilon_0\mathcal{E} + \boldsymbol{2d\mathcal{E}^2} + 4\chi^{(3)}\mathcal{E}^3 + \cdots, \end{aligned} \qquad (2-1)$$

where a_i is the i th order derivative of P with respect to $\mathcal{E}$ evaluated at $\mathcal{E} = 0$, ϵ_0 the permittivity of the medium, d the second order nonlinear effect coefficient, $\chi^{(3)}$ the third order nonlinear effect coefficient and so on.

Because of the relative low intensity of higher order effects, only the bolded second order term of Equation $(2-1)$ is considered in this section. If the incoming electromagnetic field is composed of two frequencies, ω_1 and ω_2, $\mathcal{E}$ can be written as:

$$\mathcal{E} = \mathrm{Re}\{E(\omega_1)\exp(j\omega_1 t) + E(\omega_2)\exp(j\omega_2 t)\}, \qquad (2-2)$$

where $E(\omega_i)$ is the compound amplitude of the light field with frequency ω_i. The real part of ω_i can be rewritten as:

$$\mathrm{Re}\{E(\omega_i)\exp(j\omega_i t)\} = \frac{1}{2}\{E(\omega_i)\exp(j\omega_i t) + E^*(\omega_i)\exp(-j\omega_i t)\}. \qquad (2-3)$$

Substituting Equation $(2-2)$ and $(2-3)$ into the bolded term of Equation $(2-1)$, the resulting second-order polarization term will contain expressions with five different frequency components, 0, $2\omega_1$, $2\omega_2$,$\omega_1 + \omega_2$, and $\omega_1 - \omega_2$. The 0 frequency is a steady component, but the other components suggest radiation at new frequencies due to the non-linearity of the medium.

With the help of modern pulsed lasers, the strong electric field requirement can be met, and the first reported case of second-order non-linear optics was second harmonic generation of a 694.3 nm laser in a quartz sample in 1961 [37]. Since then, many other materials have been demonstrated to have non-linear optical properties, among which β-barium borate (BBO) , potassium dihydrogen phosphate (KDP), and lithium triborate (LBO) are well-developed and widely used for laser wavelength conversion in recent years [38-44].

2.2.2 Phase matching in non-linear optical processes

Although generation of four new frequencies was shown in section 2.2.1, not all frequencies can be generated at the same time. In three-wave mixing processes, frequencies are often called ω_1, ω_2, and ω_3 in a descending order. Specifically, in an OPO, the three frequencies are called idler, signal, and pump, respectively. In any second-order non-linear processes, two conditions must be obeyed as listed below.

$$\omega_1 + \omega_2 = \omega_3, \qquad (2-4)$$

$$\boldsymbol{k}_1 + \boldsymbol{k}_2 = \boldsymbol{k}_3, \qquad (2-5)$$

where $\boldsymbol{k}_i$ is the wave vector of the electromagnetic wave with frequency ω_i. Equation $(2-5)$ is called the phase-matching condition.

In a special case commonly used in real-life setups, the three waves involved in the process are colinear. As a result, the vector sums in Equation $(2-5)$ become scalars, and can be written as:

$$\omega_1 n_1 + \omega_2 n_2 = \omega_3 n_3, \qquad (2-6)$$

where n_i is the refractive index of the ith beam. The phase-matching condition can be met in practice utilizing the birefringence crystals where light of different polarization experiences different refractive index. Taking type I phase matching in a BBO crystal as an example, a diagram showing the top view of a pair of crystals in phase match is depicted in Figure 2.2. In this scenario, two BBO crystals are oriented so that the optical axes are parallel to the horizontal plane. ω_1 and ω_2 have the same polarization which is perpendicular to the horizontal plane and are ordinary beams to the BBO crystals. ω_3 has a horizontal polarization and experiences a refractive index as a function θ, the incident angle relative to the optical axis. By rotating the BBO crystals, phase-matching condition can be met for different combination of ω_1 and ω_2. This is called critical phase matching. Notice that ω_3 is extraordinary to the BBO, therefore experiencing a spatial walk-off, as illustrated by Figure 2.2. This can be compensated by arranging a crystal of the same dimension through which. ω_3 undergoes spatial walk-off to the different direction.

Through this arrangement, efficiency of wavelength conversion can be increased and a better beam profile can be acquired [45].

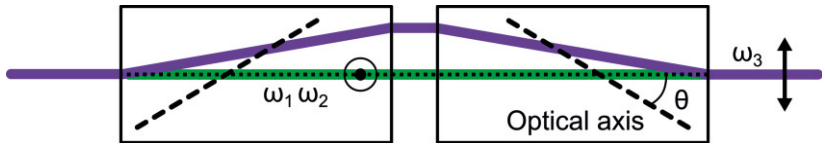

Figure 2.2: Example type I phase-matching diagram in a BBO crystal with a dual-crystal walk-off compensation arrangement (Top view).

Apart from critical phase matching, non-critical phase matching can also be achieved in some crystals such as LBO [39, 46-48]. In this scenario, the bulk of the non-linear crystal is formed by a periodic structure in which slices of the crystal are arranged at varying orientations. Wavelength tuning can be realized by controlling the temperature of such a crystal.

2.3 Lifetime of decaying processes

When excited to a higher energy level, all the excited atoms or radicals don't de-excite and emit photons at the same time. Rather, the number density of the particles at excited state goes through an exponential decay process, the rate of which depends on various parameters such as the spontaneous emission rate constant, which is an intrinsic property of the excited state, and collisional quenching rate which is connected to the surrounding environment of the particles, including surrounding species and temperature, pressure [15, 49]. Subsequently, the observed fluorescence intensity will also decay exponentially, the lifetime of which can be measured and provide valuable information. In the following sections the use of lifetime measurement for determining temperature and connection between fluorescence lifetime and particle number density measurements are addressed.

2.3.1 Lifetime-based surface phosphor thermometry

Phosphors are a class of materials that can emit light after absorbance of incident light. Among these materials, some have phosphorescence lifetimes that are sensitive to the temperature, called thermographic phosphors [50]. Typical thermographic phosphors demonstrate a decreased lifetime at elevated temperatures

due to that their non-radiative transition probability increases with increasing temperature while the radiative transition probability is not as temperature sensitive [18, 50-52]. Using this property, temperature of a surface can be measured by finding out the decay time of the thermographic phosphor applied to it, given that the lifetime-temperature dependence of the phosphor has been characterized through calibration.

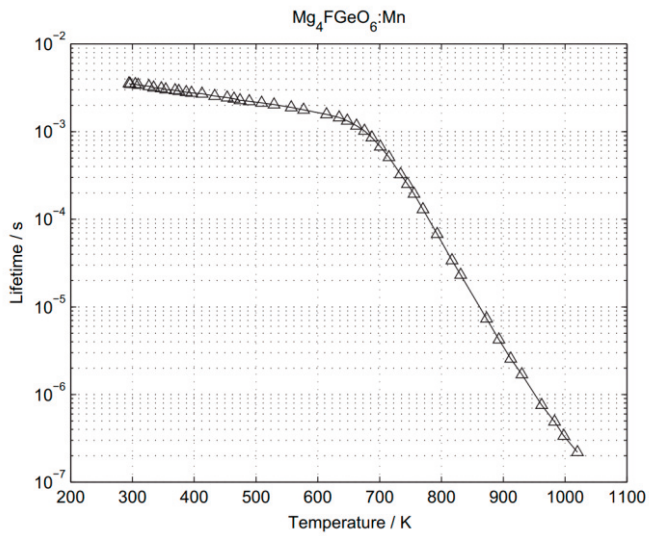

Figure 2.3: Lifetime of Mg_4FGeO_6:Mn 657 nm line as a function of temperature [50].

A example calibration curve of lifetime as a function of temperature is shown in Figure 2.3 presented by Aldén, et al [50] . It is worth noting that for each phosphor, there exists a temperature range in which the lifetime has a higher change rate relative to temperature, therefore demonstrating higher sensitivity. When using lifetime-based phosphor thermometry, the type of thermographic phosphor being used should be chosen carefully to assure appropriate sensitivity range in the desired temperature range.

2.3.2 Lifetime and number density measurements

Measuring particle number density using LIF is not a trivial task because quenching can reduce the lifetime as well as the signal intensity of LIF emission. Local species

composition, pressure, and temperature will vary the quenching rate of the measured fluorescence, making it hard to interpret the observed LIF intensity.

One way of avoiding the influence of quenching is using a short laser pulse for excitation and detect the fluorescence signal right after termination of the excitation laser. Under such circumstances, the population at the excited state can be built up before quenching starts to de-populate the state significantly. One can write that:

$$N_2(t) = b_{12} N_1^0 t, \qquad (2-7)$$

where t is the laser pulse width; $N_2(t)$ the number density of the particle at the excited state; b_{12} the rate constant for absorption that is proportional to the laser intensity and the Einstein coefficient for absorption and stimulated emission, B; and N_1^0 the initial number density of the particle at the lower state before excitation. The detected signal intensity F will then be proportional to $N_2^0(\tau)A_{21}$, where A_{21} is the Eistein coefficient for spontaneous emission and τ is the temporal width of the excitation laser pulse [15].

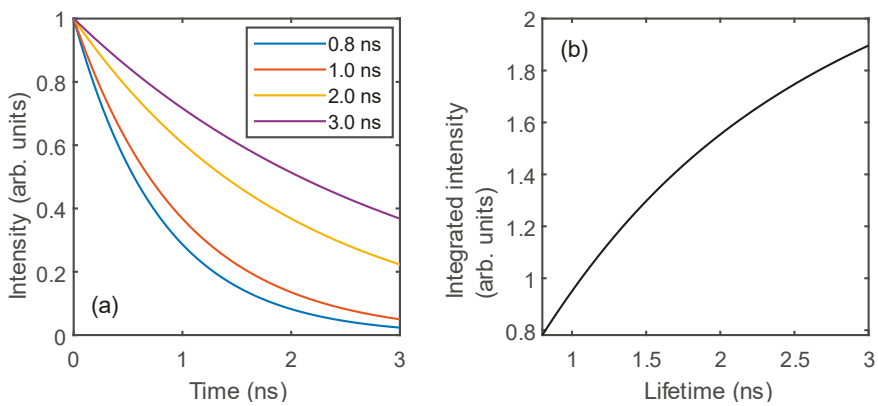

Figure 2.4: (a): Example decay curves with the same peak intensity but different lifetimes; (b): intensity of decay curves with different lifetimes integrated over a 3 ns window [53].

This, however, means that a large portion of the signal intensity gets sacrificed which is a price too high to pay in most practical measurements. To maximize signal, the decaying fluorescence signal is typically integrated over a finite gate width, which makes the expression for the total signal intensity:

$$s \sim \int_0^\infty G(t) * b_{12} N_1^0 A_{21} e^{-\frac{t}{\tau}} dt\,, \qquad (2-8)$$

where $G(t)$ is the gate function, and $\tau = \frac{1}{A_{21}+Q}$ the lifetime of the decay. Assuming that a top-hat shaped gate function of width T is used, the integrated signal s will then be:

$$s \sim b_{12} N_1^0 (1 - e^{-\frac{T}{\tau}}). \qquad (2-9)$$

In Figure 2.4, example cases are given assuming $T = 3\ ns$. As is depicted by Figure 2.4, when differences in lifetime are present, variation of integrated LIF intensity can be observed even if the excited state particle number density is the same. Equation $(2-9)$ shows that one of the approaches of tackling this problem is to perform temporally resolved measurement to find the lifetime of the fluorescence decay.

2.4 Computed emission tomography

While the detectors used for combustion diagnostics are usually 0D (e.g. PMT), 1D (e.g. spectrometers), or 2D (e.g. CCDs and CMOSs), information on the 3D field is often required to understand complicated combustion processes, necessitating measurements to reconstruct 3D information based on 2D projections. One way of achieving the goal is to scan a laser sheet to excite slices of the 3D field and perform reconstruction based on the slices [54-56]. This approach is straightforward in terms of methodology and has low demand on computational power but possesses the problem that a compromise must be made between the spatial and temporal resolution, as high spatial resolution requires more scanning which will take extra time. Another approach used widely in previous research works as well as the work in this thesis, is to simultaneously excite the volume of interest with a thick laser sheet and collect projected emission from the detection volume at various orientations. The collected data are then combined with the spatial information of the detectors to form an equation system, the solution to which is the 3D field that is measured [31-35, 57-67]. The principle of this technique is illustrated in Figure 2.5.

The tomography reconstruction algorithm used in this thesis work is described in detail in [68] and in this section, a simplified description is provided. Prior to data acquisition, a check-board pattern was placed in the detection volume and imaged from all the different viewing angles and positions. Camera matrices C can be found for each view by identification and analysis of the acquired images, which describes how points in the detection volume are projected onto the imaging sensor of the view.

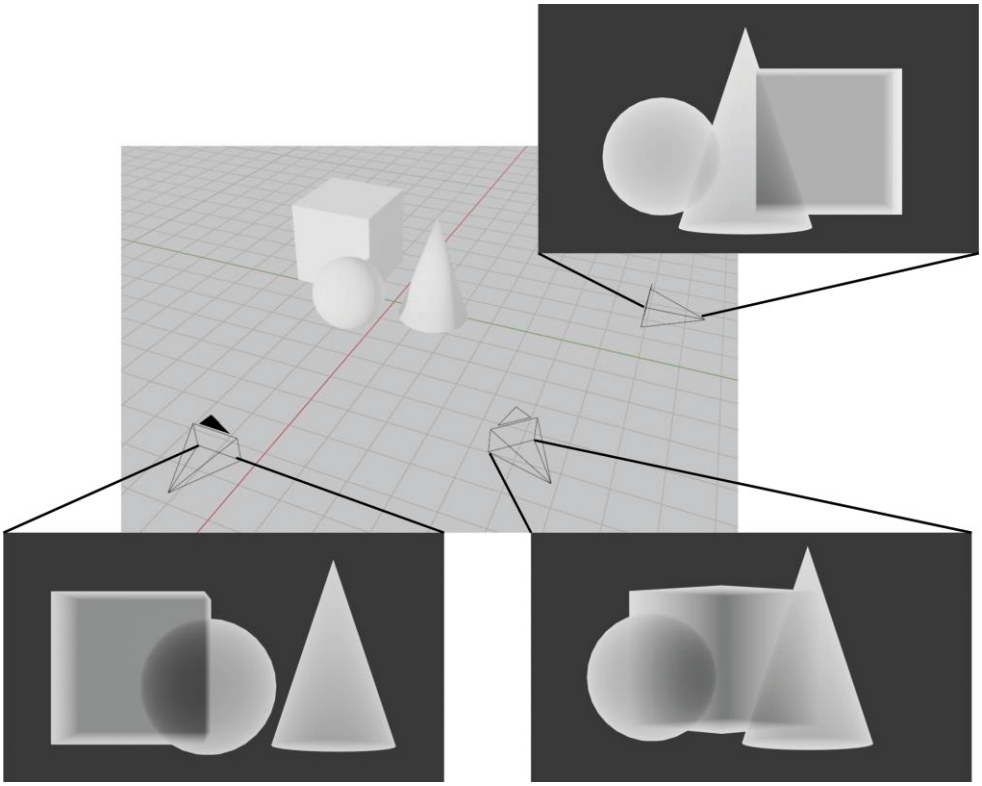

Figure 2.5: Illustration of principle of tomography, featuring the 3D field and projections from 3 viewing angles.

Discretization of the detection volume is performed, dividing the continuous volume into discrete voxels, after which a sampling method was employed to find the projection matrix for individual view A_i with the help of the Camera matrices C. Equation to solve for the detection volume can then be formed after data acquisition as:

$$\boldsymbol{A}x = b, \qquad (2-10)$$

where x represents the discretised detection volume, reshaped into a two-dimensional matrix; $\boldsymbol{A}$ the total projection matrix joined together by A_i, and b the measured results joined together the same way as $\boldsymbol{A}$.

Equation $(2-10)$ delivers the equation system that is the centre of computed tomography. The solution to the equations will produce the 3D emission field that we are interested in. In the formation of the equation system, the dimension of matrices $\boldsymbol{A}$ and b depend on the number of views from different orientations. As is

shown in [68], a greater number of views will result in reconstruction with less error. A general rule of thumb in this kind of tomography measurements is that more than 6 views are required for a reconstruction with adequate accuracy. This, however, brings challenges for high-speed LIF measurements in the UV region due to the high cost of equipment that can perform such tasks. Common solution to tackle this challenge include fibre-based endoscopes [57-59] and prism-based image splitting [31-34, 63-66]. The work of this thesis focuses on improving the later method and exploring new possibilities of multi-species tomographic LIF imaging using the same set of data acquisition equipment.

3 Quasi-modo and the customized injection seeded OPO

Burst mode laser systems, having the advantages of high repetition rate and high pulse energy compared to conventional lasers that have a typical repetition rate of 10-50 Hz, have been pursued in the field of high-speed flow research. In the past years many designs for a high-power burst laser have been proposed, among which Quasi-modo is the most recent one with the highest power available [11, 28]. In this chapter, an introduction to the layout and working principle of the system here at Lund University will be made. Following the introduction to the laser system, work towards the building of an injection seeded OPO will be described, and a detailed operational instruction will be included.

3.1 Working principles of Quasi-modo

Quasi-modo utilizes the master oscillator power amplifier (MOPA) configuration. The layout of the system present at Lund University is shown in Figure 3.1. The master oscillator in this system is a single mode diode laser that outputs a continuous wave (CW) laser beam at 1064 nm. The CW laser is amplified by a diode amplifier before an acoustic optical modulator (AOM) operating at repetition rate and gate width chosen by the user (typically ranging from 10 kHz to 100 kHz, 10 ns pulse width) shapes the original CW seed beam into a pulse train. The pulse train then enters the first amplification stage consisting of two diode-pumped amplifiers. After the first amplification stage, the pulse train is passed through an electro-optic modulator (EOM) which removes any residual intensity between consecutive pulses so that amplified spontaneous emission (ASE) is reduced in the later amplification stages.

After passing the EOM, the pulse train will go through three more stages of amplification by flash lamp pumped Nd:YAG amplifiers. To prevent damage on the gain media, the pulse train gets expanded after each stage of amplification and consequently, the amplifiers in the three flashed lamp pumped amplifying stages are equipped with Nd:YAG rods with increasing diameters of 4 mm, 9 mm and 12 mm respectively. The expansion telescopes each consists of two positive lenses to match

the beam size to the gain media diameter. Vacuum tubes are placed between each pair of positive lenses to prevent the focused high intensity pulses to generate plasma in presence of air. In the vacuum tubes, irises are placed at the beam waists. They serve as spatial filters which improves beam quality and helps suppress ASE. Optical isolators are placed between amplification stages to prevent damage of optics by back reflected light. After the final amplification stage, the pulse train is passed through a final telescope which reduces the beam diameter to 10 mm as the final output.

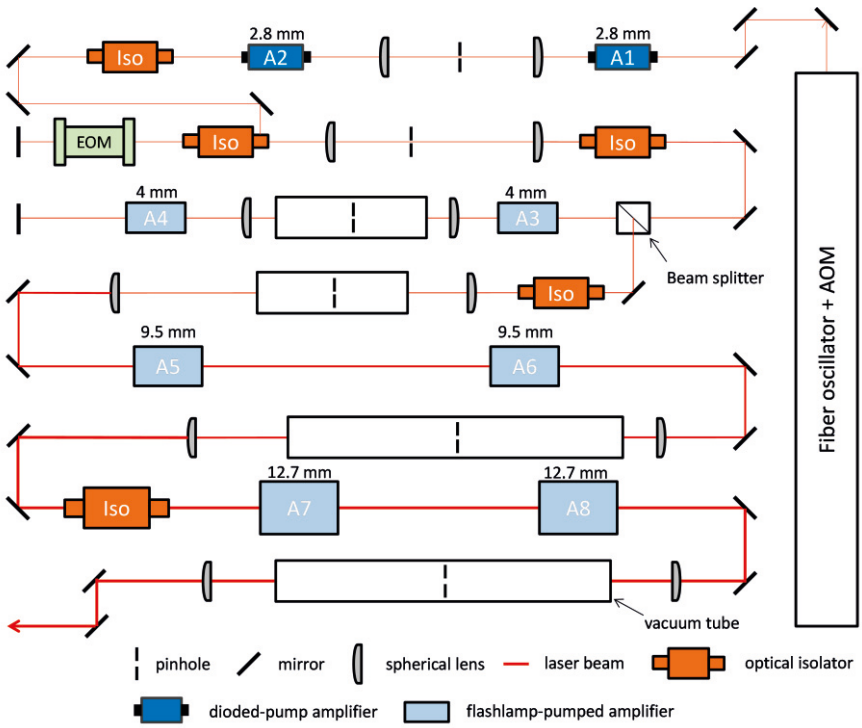

Figure 3.1: Layout of the Quasi-modo burst mode laser system at Lund University. © Spectral Energies, LLC

3.2 Timing and synchronization of Quasi-modo

3.2.1 Timing of Quasi-modo

As a high-speed burst mode laser system, correct timing is of great importance. Incorrect timing could lead to reduced energy output, damage to optical components and ultimately failure of the system. Therefore, a detailed description of the timing and synchronization is given in the current section.

The timing of Quasi-modo is controlled by an eight-channel Quantum Composer (QC) delay generator and an Agilent arbitrary waveform generator (AWG). A timing diagram of the laser under EOM gate off, internally triggered AOM, and internally triggered pulse train is shown in Figure 3.2, which is the most used settings.

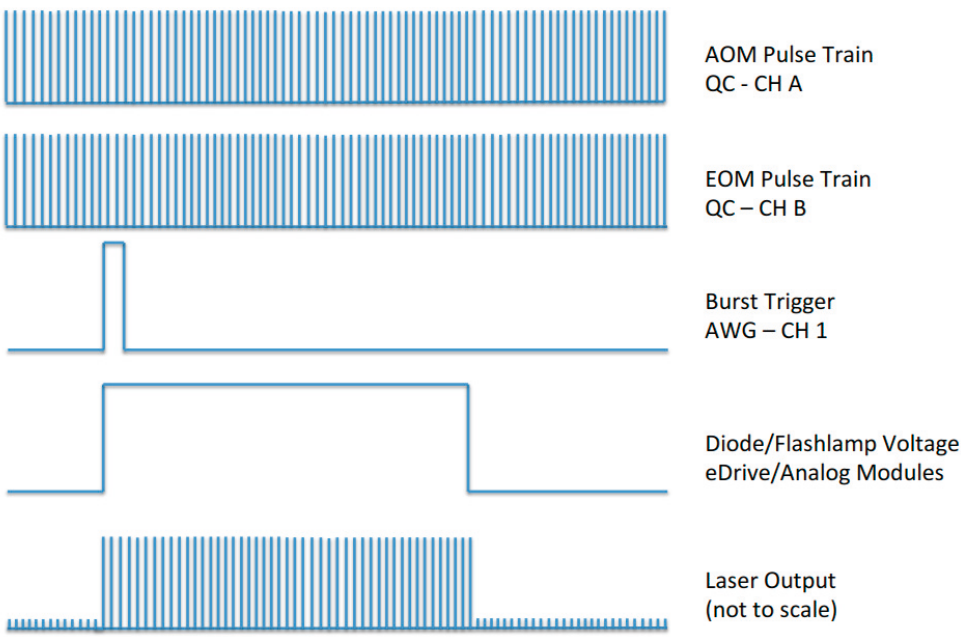

Figure 3.2: Timing diagram of Quasi-modo under normal operation mode. © Spectral Energies, LLC

Channels A and B controls the AOM and EOM respectively, and jointly govern the repetition rate of the pulse trains. By default, the width of the EOM pulse train is 1500 ns, and a delay of 1500 ns is set to channel A relative to T_0. This delay is set because of the 1500 ns rise time of the EOM. Any delay in channel A smaller than 1500 ns will result in loss in seeding laser power, and ultimately loss in the output burst energy.

The laser can also be run in a doublet mode, where the output pulses of channel C will be overlapped with that of channel A to generate laser pulse pairs at the set repetition rate, with the two pulses separated by a time t specified by the user. Note that the doublet delay set by the controlling software is set relative to T_0, so in order to get a doublet delay of t, a set value of $t + 1500$ ns should be filled in the doublet delay field in the controlling software. Under doublet operation mode, the width of channel B must also be increased to at least $t + 1500$ ns, otherwise the second pulse in the doublet could lose energy to the falling edge of the EOM.

The burst trigger generated by the Agilent AWG marks the ignition of the flash lamps, while the duration of the flashes is set by the controlling software and written to individual flash lamp control units. The period and duration of the bursts are two vital parameters ensuring the safe operation of the laser. A longer burst duration set to the flash lamps will result in a greater number of pulses in one burst, and consequently a higher stress on the optical components. When aligning, a burst width of approximately 2 ms is used. In typical experimental scenarios, burst widths of less than 3 ms are used. Extra care in alignment to avoid hot spots must be taken when a wide burst width is used. Continuous operation of the flash lamps will heat up the Nd:YAG rods, creating thermal lensing effect that will create hotspots in the beam profile. Therefore, a burst period of minimum 8 seconds must be used when running the laser and should be increased with increased pumping power. When running at full power, at least 20 s must be set between two bursts.

3.2.2 Synchronization with cameras and oscilloscopes

Synchronization of high-speed cameras and intensifiers to Quasi-modo is described in this section using a Photron Fastcam series high-speed CMOS as an example. A diagram of the setup is shown in Figure 3.3.

Before experiment, resolution setting on the high-speed camera must be checked to make sure that data can be captured at the desired repetition rate. With the camera set to external synchronization mode, the channel E output at the back of rack 1 of Quasi-modo is connected to the sync in connector in the high-speed camera's I/O ports. The channel 1 output from the AWG is connected to the camera's trigger TTL in port. One out of the three general out channels of the high-speed camera outputs is set to "expose pos", outputting a high level when the COMS is acquiring data. This channel is used to trigger the high-speed intensifier control unit, and from the

control unit a synchronized tigger signal is sent to the intensifier. With this setup, the trigger output from AWG channel 1 marks the start of acquisition, and both the high-speed camera and the intensifier are synced to the AOM signal. Delay in the camera and intensifier must be carefully adjusted to make sure of proper exposure upon arrival of the laser pulses.

On some occasions, it can happen that the delay in the high-speed camera between synchronization trigger in and camera gate open exceeds the delay of 1500 ns set by QC channel 1 so when the camera gate opens the laser pulse has already been missed. In these cases, an extra delay can be set to QC channel A to match the delay of the camera gate. One must keep in mind to add the same delay to QC channel B, otherwise the pulse train will suffer an energy loss due to the falling edge of the EOM.

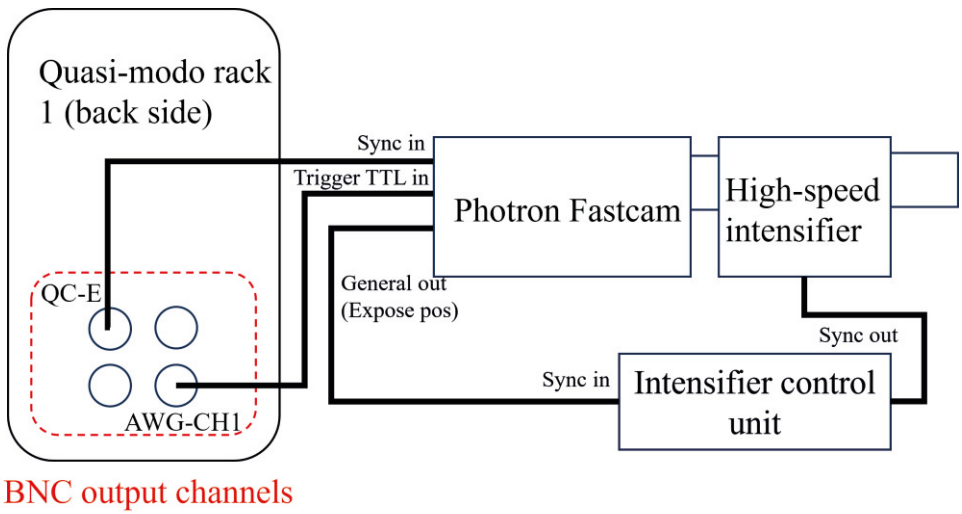

Figure 3.3: Example diagram of Quasi-modo synchronized to a high-speed camera and high-speed intensifier.

3.3 Wavelength conversion of Quasi-modo

As is discussed in section 2.1, most often a specific laser wavelength is needed to excite species of interest in research. Therefore, two devices to convert the fundamental 1064 nm output from Quasi-modo to other wavelengths are utilized in

the system here at Lund University, the harmonic generator unit (HGU), and the injection seeded OPO, the design of which was first reported by Halls, etc. [33].

In both wavelength converting devices, second order nonlinear optical effects are used for the generation of new wavelengths.

3.3.1 The harmonic generator unit

The HGU of Quasi-modo has two detachable wavelength conversion units and can convert the fundamental beam of 1064 nm to 532 nm, 355 nm and 266 nm. A layout of the HGU is shown in Figure 3.4 and a brief description is given in this section.

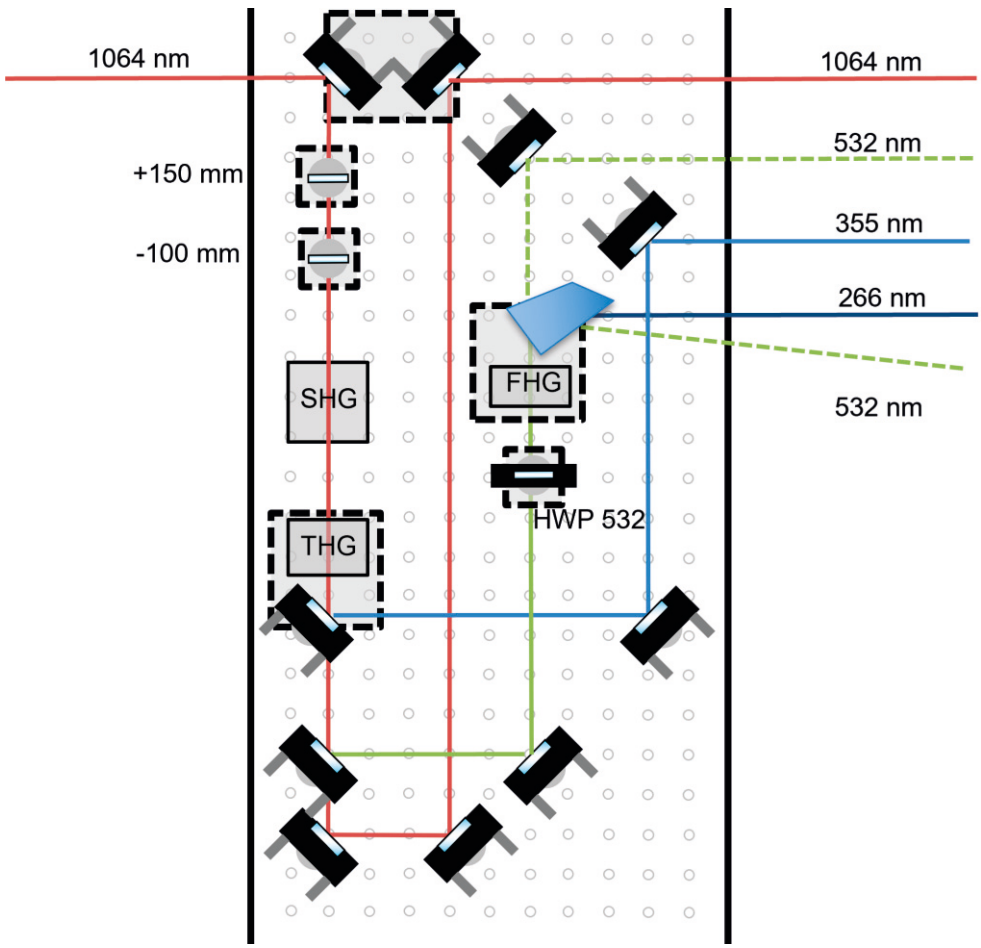

Figure 3.4: Layout of the Quasi-modos's harmonic generator unit. © Spectral Energies, LLC

When harmonic generation is not needed, the mirror pair shown in the upper left corner of Figure 3.4 can be removed, and 1064 nm directly exits the HGU without interacting with other components. When placed in position, the mirror pair will guide the 1064 bursts to a telescope that reduces the diameter of the beam, before passing the beam into the second harmonic generator (SHG). The SHG has a noncritical phase matching type I LBO crystal whose temperature is controlled by an oven. If the third harmonic generator (THG) is in place, the frequency-doubled 532 nm beam and the residual 1064 nm beam will interact in its type II LBO crystal, producing 355 nm laser pulses. The THG crystal is angularly phase matched at the vertical direction. It is worth noting that when working at lower repetition rates (≤20 kHz), the optimum doubling temperature of 149.7 ˚C will cause a too high doubling efficiency, depleting the 1064 nm pulse energy, therefore causing a decrease in the conversion efficiency for 355 nm pulses. As a result, temperature of the SHG crystal must be increased to get optimum 355 laser energy.

If generation of 266 nm light is not needed, the 532 nm beam will continue propagating and leave the HGU at the exit next to the 1064 nm. With the presence of the fourth harmonic generator (FHG), the 532 nm will be further frequency doubled to generate 266 nm light, and both wavelengths are sent into a Pellin-Broca prism and are separated further downstream.

3.3.2 Injection seeded OPO

Compared to the HGU which can only convert the fundamental wavelength of 1064 nm to its harmonics, the injection seeded OPO is a more flexible way of converting laser wavelength. A traditional dye laser does not have the capability to circulate the dye fast enough, resulting in decreased conversion efficiency when pumped by laser pulses at repetition rates much higher than 10 Hz and pulse energy in the order of 100 mJ [69]. Although successful demonstration has been made for a prototype dye laser system pumped with burst mode laser to generate UV laser pulses [70], a complicated customized dye circulation system is needed. In the balance of performance and cost effectiveness, the injection seeded OPO solution was chosen in the Lund University system.

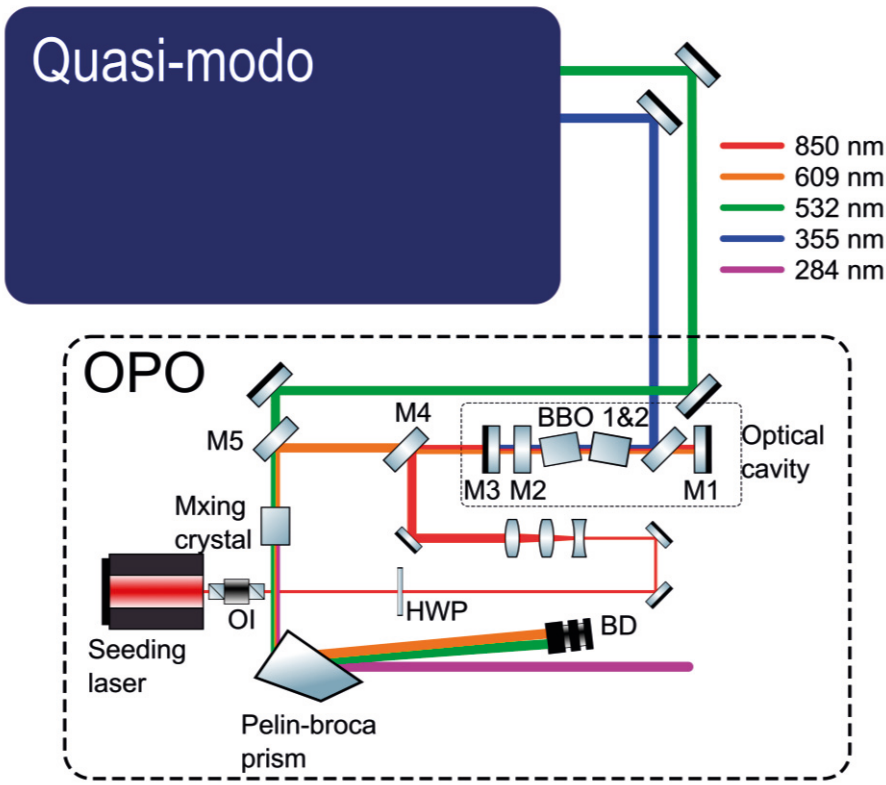

Figure 3.5: Schematic drawing of the customized injection seeded OPO. M1-5: mirrors; BD: beam dump; HWP: half-wave plate; OI: optical isolator. Illustrations of the optical components by ComponentLibrary created by Alexander Franzen licensed CC BY-NC 3.0.

A schematic drawing of the OPO is shown in Figure 3.5. 355 nm laser pulses are directed into the OPO cavity by a 45˚ 355 high reflector. Three mirrors marked as M1-3 form the optical cavity. The right most mirror (M1) is coated to reflect wavelengths within ranges 600-640 nm and 820-860 nm. M2 is coated to transmit 355 nm and have 20% reflectance within 600-640 nm and 820-860 nm, serving as the output coupler. M1 and M2 forms the doubly resonant cavity for signal and idler. M3 lies to the left most of the cavity, coated to transmit in the visible and reflect 355 nm, creating a double pass of the pump beam to boost the conversion efficiency. In the cavity, two type I beta barium borate (BBO) crystals cut at $\theta = 32°$ are placed

in a walk-off compensation configuration. For OH excitation, the 355 nm pump laser pulses are converted to signal wavelength of 609 nm and idler wavelength of 850 nm.

In order to minimize the spectral width of the output wavelengths, a single mode diode laser from Sacher was used as injection seeding. And an optical isolator was used to protect the laser from back reflections, and a half-wave plate was used to make the seeding laser vertically polarized as needed in the cavity. The single mode CW seeding beam at the idler wavelength is sent through a series of negative spherical lens and positive cylindrical lenses to be formed into a circular beam with a diameter of 8 mm, matching that of the pump beam. After the shaping, the seeding beam is aligned with the cavity by M4 and sent into the cavity through the output coupler. M4, coated with an anti-reflection coating at the signal wavelength and high reflectance at the idler wavelength, also prevents the idler from propagating further downstream into the mixing crystal. The signal, after passing through M4, is combined with the residual 532 nm coming from the Quasi-modo HGU and sum frequency converted by another BBO crystal ($\theta = 43°$, type I) to generate 284 nm for OH excitation. The three wavelengths are then separated by a Pellin-Broca prism and pure 284 nm pulses are obtained.

3.4 Alignment of the injection seeded OPO

Precise alignment is vital to the operation of the injection seeded OPO. When working with the OPO, together with former colleague Panagiota Stamatoglou, routines for aligning and operating the OPO were established in different scenarios and are described in detail in the current section. In cases where the alignment is off and recovery takes too much effort, removing all cavity components from their posts and rebuild the cavity could be more efficient. Practices under such circumstances are given in section 3.4.1. Some hints when operating the OPO are provided in section 3.4.2.

3.4.1 Rebuild of the cavity

In a rebuild of the cavity, the diode seeding laser was found to be a good coherent light source whose interference could be used as an indicator of a parallel cavity. Also used in this procedure are the IR viewer used for Quasi-modo alignment, a 50:50 cubic beam-splitter, and a USB spectrometer for rough monitoring of the output wavelength. Detailed alignment steps are given as follows:

1) To prepare for the rebuild, all optical components including cavity mirrors, BBO crystals, mixing crystals, Pelin-Broca prism and beam shaping optics for the seeding laser are removed from the posts. The seeding beam is aligned

through the cavity at a centred position and will serve as reference for the rest of the alignment. A holder with a detachable pin hole is placed in the HGU as close to the THG as possible, whose position is adjusted for the 355 pulses to pass through its centre.

2) M3 is placed back to its holder. The angle of M3 should be adjusted so that the back-reflected seeding beam goes back into the optical isolator. After fixing M3, the 355 nm laser, run with diode amplifiers and 4 mm flash lamp amplifiers on, is aligned to overlap with the seeding beam upon hitting M3, and the back reflection of the 355 nm light should go through the pin hole. A schematic illustration of the procedure is included in Figure 3.6. This is an important step in that the reflected 355 nm pulses must be steered clear from any metal surfaces in the HGU to prevent them from generating dust that will accumulate on optical surfaces and cause damage.

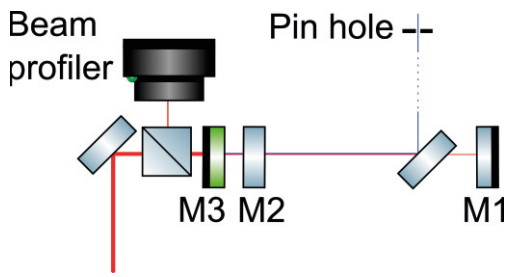

Figure 3.6 Schematic drawing of the OPO cavity during alignment (HGU left out in the drawing).

3) The 50:50 cubic beam splitter is placed between M4 and M3, and the IR viewer is placed between the OPO and Quasi-modo to observe the reflected beam profiles. Note that the beam splitter must be put so that the light leaving the cavity is sent into the IR viewer. On the IR viewer, two beams can be observed at this point, being the reflection from M3 and a reflection from an existing surface of the beam splitter. The angle of the cubic beam splitter is adjusted so that the two profiles overlap, and low-order equal inclination interference is observed.

4) M2, M1 and BBO crystals are installed in order, and the angle of each component must be adjusted until satisfactory interference pattern is observed on the IR viewer before the next one is installed. In this way, a parallel optical cavity and pump beam path almost perpendicular to the cavity is acquired.

5) Next step is to adjust the phase matching angle of the crystals. Pulse energy in the 355 nm beam is increased compared to step 2), and the two BBO crystals are rotated about the vertical axes. At this stage a mirror should be put at the position of the Pelin-Broca prism, and the output of the OPO is aligned to a scattering surface such as the surface of the energy meter. The collection fibre for the USB spectrometer is placed to collect the scattered light. From experience, the crystals are close to phase matched at about 520-530 nm when aligned at a perpendicular pump pulse incidence. When installed, the optical axes of the two crystals must be inspected to make sure that the walk-off compensation arrangement is achieved. During wavelength tuning of the OPO, the two crystals are to be rotated in opposite directions. Typical operation procedure is to rotate one crystal first while observing the output wavelength. If pumped at sufficient energy, the 355 nm laser will be downconverted to different wavelengths at the two crystals. Tune one crystal until a noticeable shift in signal wavelength towards the red occurs and tune the other to gain phase matching again. When both crystals are correctly phase matched, a drastic increase in output intensity and decrease in threshold energy can be observed. The angular tuning steps are to be repeated until phase matching at roughly the desired wavelength is achieved.
6) With the mirror replacing the Pelin-Broca prism, 532 nm pulses are sent through, and both beams are propagated further downstream to check for overlap. Once the two wavelengths are overlapped well enough, the Pelin-Broca prism and the mixing crystal can be introduced into the beam path.
7) Finally, beam shaping optics for the seeding laser are installed, and their position and height are adjusted so that the seeding laser reaches the optical cavity with the correct beam size at the right position and angle. Now a rebuild of the cavity is finished.

3.4.2 Daily operation tips

When starting the laser for the first time each day, a series of check-ups must be carried out. After fixing the position of the holder for the pin hole as mentioned in section 3.4.1, it should remain untouched and will serve as alignment reference. The Quasi-modo is to be run at low energy (4 mm amplifiers on 490 V @ 50-100 kHZ) and the 355 nm pulses are checked to pass through the centre of the BBO crystals and their reflections pass through the pin hole. The pulse energy is the gradually increased until low level of output can be observed from the OPO. Use the USB spectrometer to check that the output wavelength is roughly in the desired range.

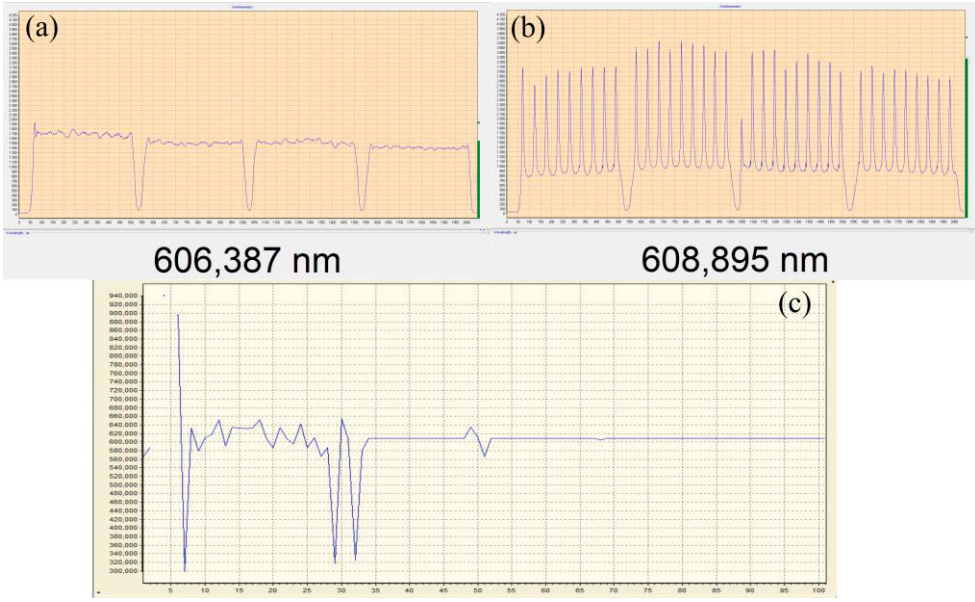

Figure 3.7: Results from the wavelength meter. (a): single pulse train result under unseeded operation (b): single pulse train result under seeded operation (c): measured wavelength vs time plot.

Seeding laser is turned on and alignment of the seeding beam is checked. The OPO is pumped at a stable level (pump energy more than twice the threshold energy) and the output is picked up by a fibre to send to a HighFinesse high-precision wavelength meter. Examples of output patterns from the wavelength meter are shown in Figure 3.7. Without seeding, the signal wavelength output has a spectral bandwidth that is beyond the detection limit of the wavelength meter, as shown in Figure 3.7(a). When successfully seeded, a distinct interference pattern can be observed, and the wavelength meter is able to report the correct output wavelength, as illustrated by Figure 3.7(b). The wavelength vs time plot can also be checked. When successfully seeded, the measured wavelength of the output pulses remains stable. Figure 3.7(c) shows the difference in measured wavelength over time between unseeded operation (first half of the plot, where the reported wavelength is unstable and varies over a wide range) and seeded operation (second half of the plot, reported wavelength stays stable at 608.895 nm).

Confirmation of spatial overlap between the 609 nm and 532 nm should be made with a mirror replacing the Pelin-Broca prism. After the confirmation, the Pelin-Broca prism can be introduced back to the beam path, and the 609 nm and 532 nm pulses are terminated by a beam dump. A UV fluorescence card can be used when the mixing crystal is tuned to see the 284 nm output.

4 Towards investigation of spark plug wear using nickel LIF

In spark-ignited (SI) internal combustion engines, spark plugs are used to create plasma that ignites the fuel-air mixture in the combustion chamber at the end of the compression stroke. Spark plugs suffer from a harsh working environment because as the plasma is initiated, instantaneous current can peak at a few hundred amperes while the gas temperature between the electrodes can reach more than 3000 K [71]. The electrodes experience significant heating as well as bombardment by the accelerated charged particles. As a result, the spark plug gets eroded each time ignition is initiated, which introduces loss of engine performance and increased risk of misfiring as the wear accumulates [72, 73]. In modern heavy-duty natural gas vehicles, a spark plug lifetime of 1000-4000 hours is typical, while a lifetime of more than 8000 h is desired by the industry to reduce downtime due to maintenance and corresponding economical loss [73].

The work in this thesis aims to lay foundation for a novel approach to diagnose spark plug erosion based on LIF of Ni atoms in the spark gap, which has the potential to provide temporally resolved data on electrode erosion rate, helping the industry in finding a more efficient and less erosive driving strategy for creating the spark discharge.

4.1 Experimental setup

4.1.1 The spark plug wear test rig

A dedicated spark plug wear test rig was designed and manufactured by Swedish Electro Magnets AB (SEM AB), in which spark discharges can be generated in a repeatable manner, and parameters of the spark plug such as the electrode separation, electrode material and voltage driving profile can be changed at will. A figure of the test rig is shown in Figure 4.1.

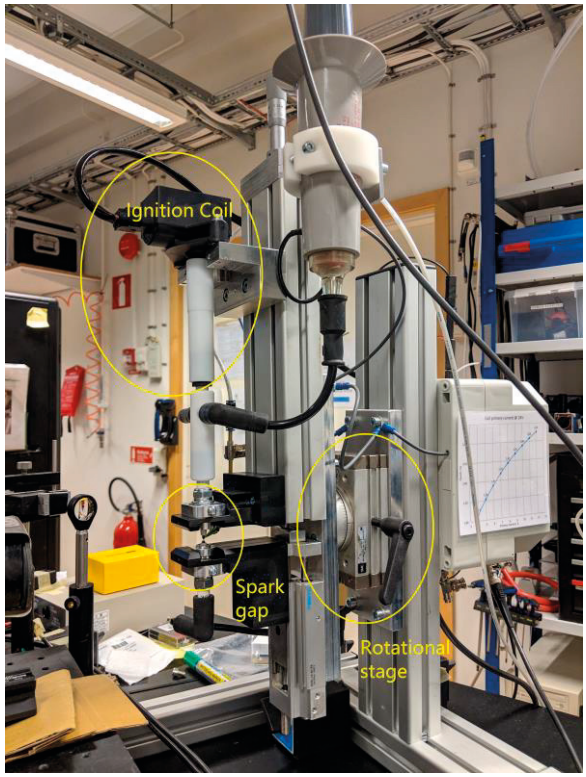

Figure 4.1 Picture of the spark plug electrode erosion test rig.

Mounted on a structure made from aluminium profiles, two standard J-gap spark plugs with their ground electrodes removed serve as the spark electrodes. The spark discharge is created between the exposed central electrodes of the two spark plugs. The bottom electrode is grounded and serve as the anode, while a negative driving voltage is applied through an ignition coil attached to the top electrode which serves as the cathode. The distance between the two electrodes can be adjusted by a translation stage. The ensemble is attached to a rotational stage allowing for adjustment of angle on the vertical plane.

4.1.2 Optical set-up

A schematic drawing of the optical setup is shown in Figure 4.2 (a). The optical diagnostics have been carried out in three stages. In stage one, passive spectroscopic study on the spark discharge's spontaneous emission was conducted. In this stage, a spectrometer (Princeton Instruments Acton SpectroPro 2300i) and an intensified

charge-coupled device (ICCD) camera (Princeton Instruments PI-MAX II) were used to register the emission spectrum of the spark discharge. An achromatic lens (f=100 mm, *f*/2.0, B. Halle) was used to collect the emission signal to the entrance slit of the spectrometer. As shown in Figure 4.2 (b), the spectrometer assembly was rotated for the entrance slit to be imaged to the spark gap perpendicular to the spark discharge.

Following the passive detection of the emission spectrum, an excitation scan was carried out to find potential excitation wavelength for LIF detection of Ni atoms present in the spark gap. In this stage, a tuneable picosecond laser system produced by EKSPLA (UltraFlux FT405) was used as the excitation source. On the detection side, an intensified complementary metal-oxide semiconductor (ICMOS) camera (Andor iStar) was used for data collection together with the Princeton Instruments spectrometer. The 90 ps wide pulses were focused into the spark gap by a 100 mm focal length UV fused silica (UVFS) lens. The excitation wavelength was scanned from 210 nm to 340 nm with a 0.5 nm step size, and a more detailed scan was done between 327.8 nm and 337.7 nm with a 0.1 nm step size while the resulting emission in the spectral range 338.8 nm to 353.6 nm was monitored by the ICMOS camera.

The excitation scan during stage two revealed an ideal excitation wavelength of 336.94 nm after wavelength calibration. In stage three, a study on the LIF lifetime at the selected excitation wavelength was performed to pave the way to Ni atom population detection by PLIF. For this measurement, a slit was put at the exit focus of the spectrometer. With the width set to 3 mm, the exit slit allowed passing of a spectral width of about 7.4 nm. The centre wavelength of the allowed spectral range was set at about 345.0 nm by turning of the grating. The signal existing from the spectrometer was picked up by a Hamamatsu R5916U-50 MCP-PMT, and the temporally resolved decays of the fluorescence was recorded by an oscilloscope (Teledyne LeCroy WavePro 604HD 6 GHz 20 GS/s). The delay between the initiation of the spark discharge and the laser pulse was scanned from 50 µs to 3500 µs at a step size of 50 µs.

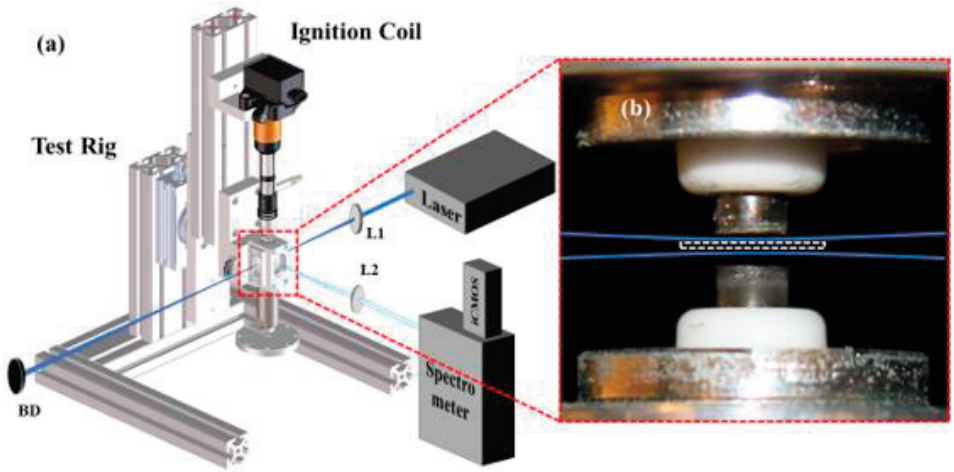

Figure 4.2: Schematic drawing of optical setup for spark plug electrode erosion detection. (a): Overview of the setup; (b): close-in view on the electrode pair, blue line indicating path of the excitation laser and white dashed rectangle representing the detection volume of the spectrometer [74].

4.2 Results

4.2.1 Passive emission spectroscopy study

In this study, an electrode combination of iridium as cathode and nickel as anode has been used. An inductive ignition coil charged for 2 ms initiated a discharge that lasted for approximately 3 ms. In Figure 4.3, an example of the voltage and current traces of a spark discharge is shown.

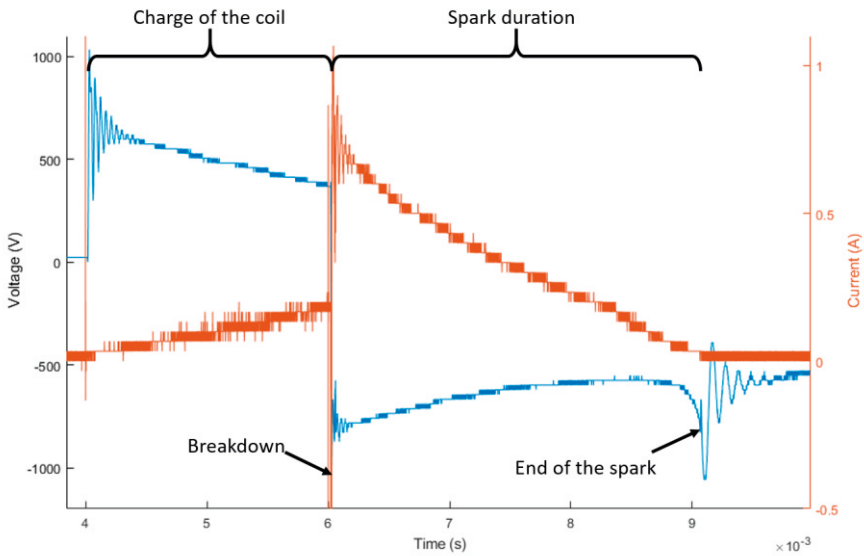

Figure 4.3: Example voltage and current traces of an inductive spark discharge [75].

Due to the randomness in the position of the spark discharges, loss of signal intensity and even absence of emission signal can be observed as the discharges are frequently generated outside the plane of vision of an entrance slit oriented parallel to the discharge channel. The solution to this problem was to rotate the spark generation assembly by 90˚, making the plane of interest perpendicular to the plasma channel as described in section 4.1.2. By adopting this arrangement, spatial resolution was also gained along the horizontal direction. In Figure 4.4 (a), a close-up photo of the two electrodes used in the test is shown. Two lines are drawn in Figure 4.4 (a), representing the two planes of interest on which emission spectra were taken.

Results of the emission spectroscopy were shown in Figure 4.4 (b), (c) and (d). On each plane of interest, a total number of 500 spectra were recorded, each with a gate width of 3 ms. Figure 4.4(b) and (c) show the normalized sum of spectra taken at plane close to the iridium electrode and plane close to the nickel electrode, respectively. Background was also taken by averaging a region in each spectrum where signal was not present and subtracted from the original data. For demonstration and comparison purposes, example spectra were plotted from single rows taken from Figure 4.4 (b) and (c) in Figure 4.4 (d).

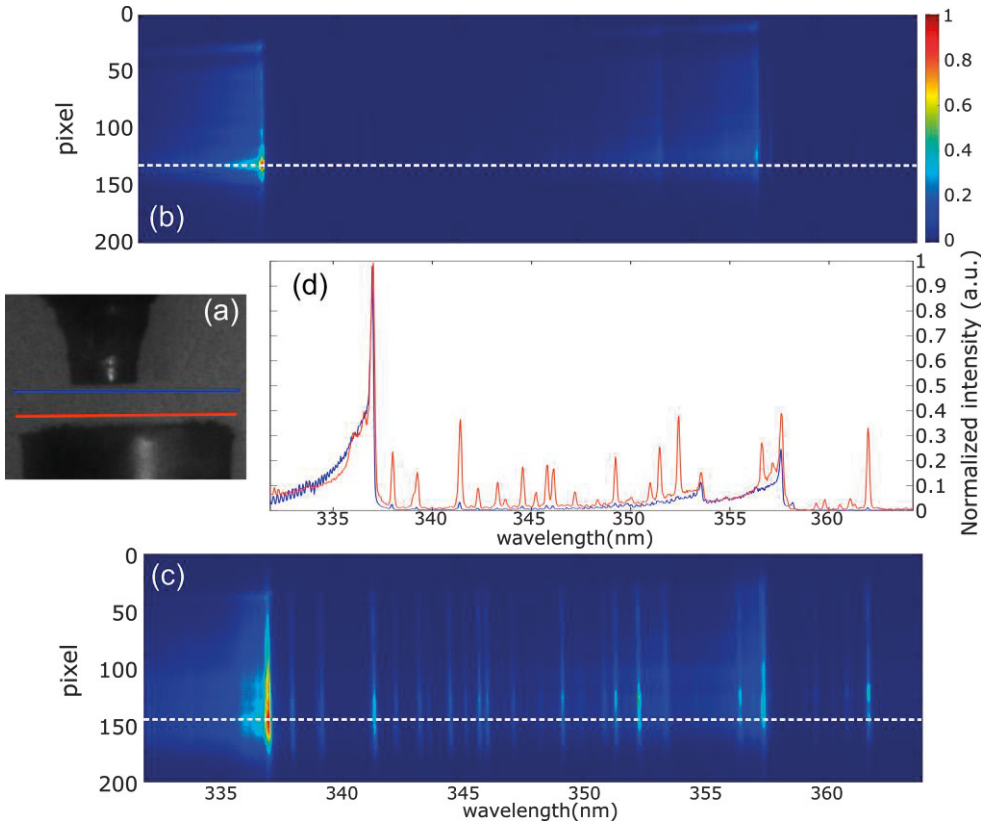

Figure 4.4: Emission spectra taken from the spark discharge. (a): Close-up photo of the electrodes, colored lines indicating the planes of interest. Blue is plane taken close to the cathode (Ir), red close to anode (Ni); (b), (c): Sum of 500 2D spectra taken at each plane of interest; (d): Spectra taken from selected rows from (b) and (c), as indicated by the dotted white lines.

Comparing the spectra taken at both planes, common features are three emission bands with peaks at 337.1 nm, 353.7 nm and 357.7 nm. Appearance of such feature are also reported in other literatures where spark discharges were generated in similar setups [76-79], and they are identified to be the C→B (0,0), (1,2) and (0,1) transitions of Nitrogen, respectively. The emission band of Nitrogen C→B has been well observed in plasma research and has been used widely in diagnostic of plasmas such as vibrational temperature characterization [80-82]. Less studied are the sharp emission lines appearing in the spectral range of 338 nm to 365 nm. The observed transitions were cross-checked with NIST database and were identified as emission from Ni. Similar observations have been made in [78].

A large difference in atomic Ni emission intensity can be seen between the spectra taken close to the Ir electrode and Ni electrode, as is illustrated in Figure 4.4(d), which is an indication that the occurrence of Ni atoms in the spark gap is highly local. This behaviour follows the description of electrode erosion due to evaporation proposed by Coulombe, et al. [83, 84]. In search for an in-situ, real-time optical diagnostic approach for electrode erosion, the observed Ni emission lines showed great potential. Specifically, the spectral region that is about 10 nm wide centred around 343 nm has very low background emission present and could serve as an ideal detection window for optical diagnostics.

4.2.2 Excitation scan for Ni atoms

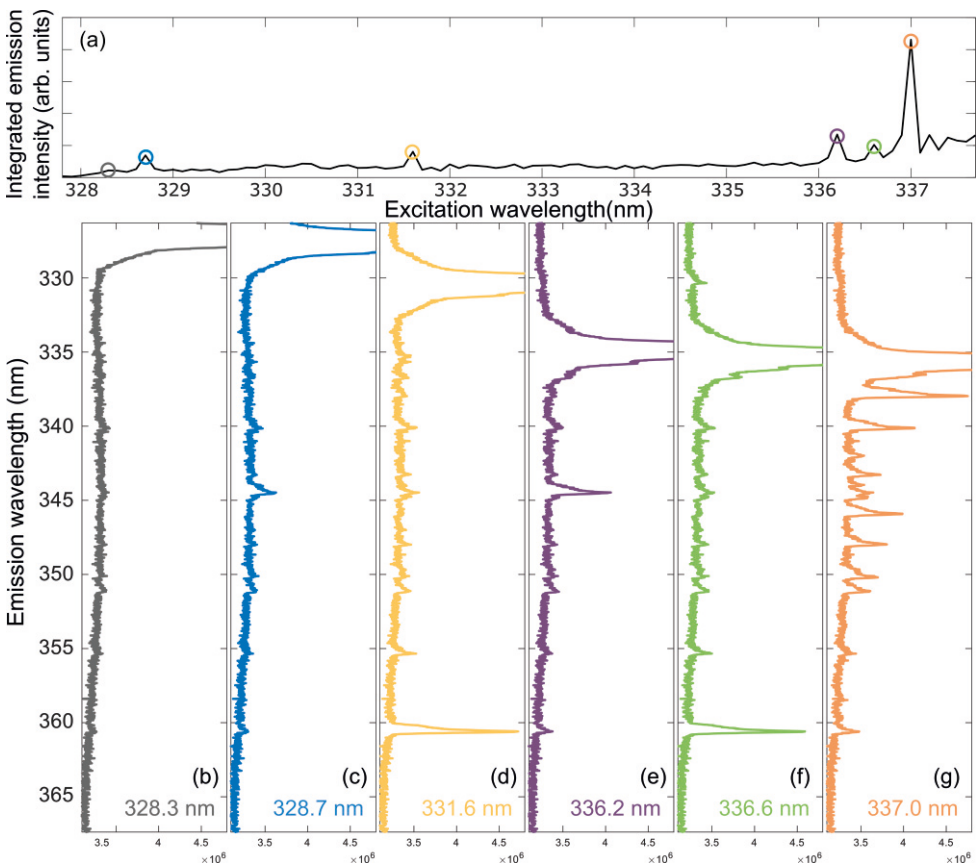

Figure 4.5: (a): Integrated LIF emission intensity as a function of excitation wavelength; (b): Emission spectrum example absent of LIF emission; (c)-(g): emission spectra present with LIF emission. Saturated peaks observed in (b)-(g) originate from the excitation laser.

In search for an optimum wavelength for LIF detection in the 338 nm to 348 nm detection window, an excitation scan was performed from 327.8 nm to 337.7 nm at a step size of 0.1 nm. A summarization of the excitation scan is shown in Figure 4.5. At each excitation wavelength, the recorded spectrum was integrated in the spectral range between 338 nm and 353 nm, and the integrated intensities were plotted against the excitation wavelength in Figure 4.5 (a). From Figure 4.5 (a), several excitation wavelengths can be observed where the integrated emission intensity demonstrated obvious increase compared to the neighbouring wavelengths, thus indicating presence of LIF signal. The observed wavelengths are 328.7 nm, 331.6 nm, 336.2 nm, 336.6 nm, and 337.0 nm. The emission spectra recorded at the above-mentioned wavelengths are shown in Figure 4.5 (c)-(g), and as a reference, Figure 4.4 (b) shows a spectrum recorded at 328.3 nm excitation wavelength which doesn't correspond to a Ni absorption line.

With the laser tuned to 337.0 nm central wavelength, the highest integrated LIF intensity was observed, whose emission spectrum is shown in Figure 4.5 (g). A cross-reference with the NIST database suggests that the laser light was absorbed by the Ni atoms at 336.957 nm, exciting the Ni atoms from their ground state to the $3d^9(^2D)4p^\circ\ J = 3$ state [85-88]. Multiple LIF emission lines emerge from the excitation at this wavelength, and most intensities fall in the detection window found in the previous spectroscopic observation. An energy level diagram in Figure 4.6 illustrates the levels involved in the excitation and emissions. According to the NIST database, the upper state of the excitation $3d^9(^2D)4p^\circ\ J = 3$ has not been assigned a term, and the two largest components of its eigenvector are $3d^9(^2D)4p\ ^3D_3^\circ$ and $3d^8(^3F)4s4p\ ^5F_3^\circ$, each takes up a percentage of about 30%. Limited by the resolution of the spectrometer, not all transitions were included in Figure 4.6. In cases where multiple lines are too close to identify, only the transition closest to the wavelength of the highest observed intensity was shown. Approximately half of the observed transitions originated from the $3d^9(^2D)4p\ ^3D^\circ$ and $3d^8(^3F)4s4p\ ^5F^\circ$ states, and in the other cases, the observed transitions originated from the $3d^9(^2D)4p\ ^3P^\circ$ and $^3F^\circ$ states, suggesting the occurrence of collisional relaxation before the radiative transition. It is worth pointing out that the emission observed at 345.8 nm was emitted by the transition from $3d^9(^2D)4p\ ^3F_3^\circ$ to $3d^9(^2D)4s\ ^3D_1$, whose upper level has a higher energy than the upper levels of the excitation. This suggests that collisions of the excited Ni atoms with the high-energy particles in the plasma channel have pumped the excited Ni atoms to an even higher level.

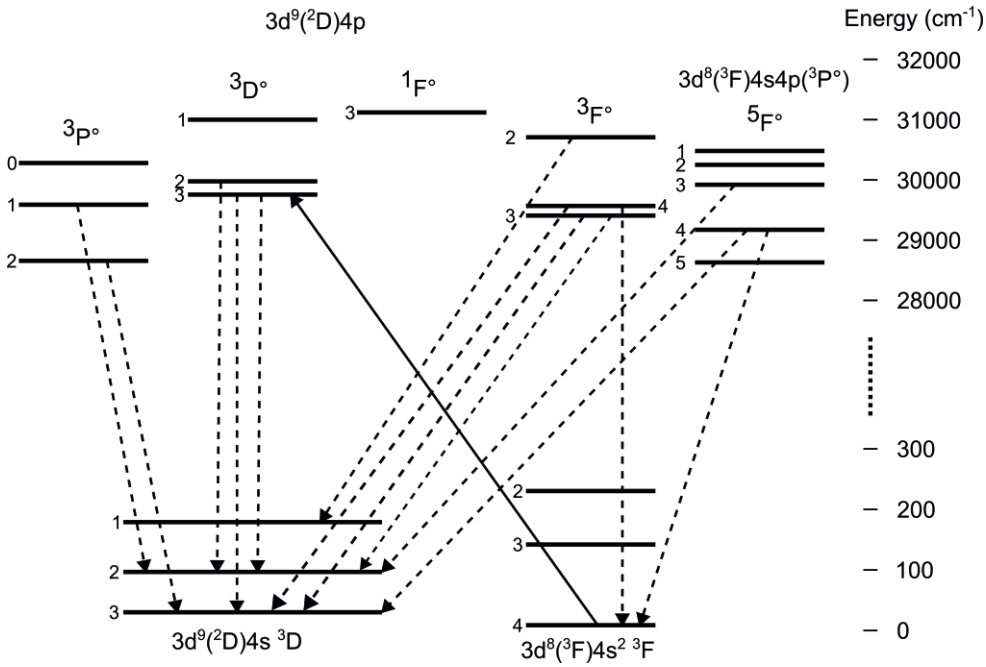

Figure 4.6: Energy diagram of the Ni LIF transitions observed at 337.0 nm excitation.

In Figure 4.5 (c)-(f), emission spectra excited by four other wavelengths are also included. In these cases, LIF emission was also observed, but the emission spectra demonstrated different characteristics. In all four excitation scenarios, there existed one transition in which most of the intensity contribution was concentrated, as opposed to the much more even distribution of energy in a much greater number of transitions when excited by 337.0 nm. With the help of NIST database [85], the upper and lower levels of the four transitions were found. In the cases shown by Figure 4.5 (d) and (f), the upper level was the same, which is $3d^9(^2D\ )4p\ ^1F_3^\circ$. The most intense emission line observed in the two cases was located at wavelength of 361.92 nm, originating from the same upper level down to the $3d^9(^2D\ )4s\ ^1D_2^\circ$.state at 3409.937 cm^{-1}. This transition is a singlet-to-singlet transition, as opposed to most of the other strong lines observed in the 337.0 nm excitation case that are triplet-to-triplet transitions. In the other two cases shown in Figure 4.5(c) and (e), a common upper level was also shared by the two excitation wavelengths. Though in this case, de-excitation from the $3d^9(^2D\ )4p\ ^3F_2^\circ$ state to the $3d^8(^3F)4s4p\ ^5F_3^\circ$ state happened before the radiative transition down to the $3d^9(^2D\ )4s\ ^3D_2$ state yielding the strongest emission at 345.289 nm. In addition, it is worth pointing out that a blue-shifted LIF emission line was observed when excited by 336.6 nm light. This

weak, blue-shifted emission was the result of transition from $3d^9(^2D)4p\ ^1F_3^\circ$ to $3d^9(^2D)4s\ ^3D_2$.

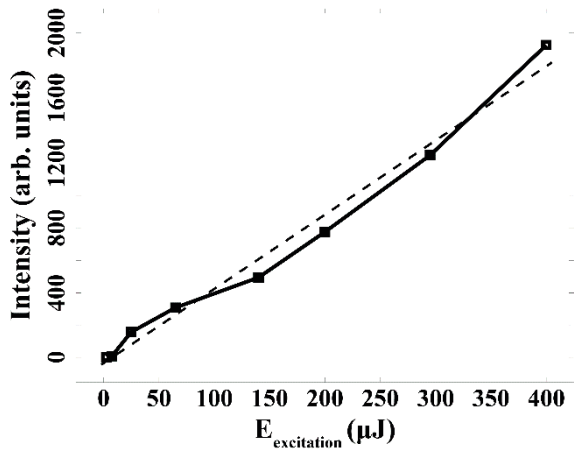

Figure 4.7: Integrated LIF intensity as a function of laser pulse energy, excited at 337.0 nm [74].

Through the excitation scan, an optimum excitation wavelength of 337.0 nm was found. An additional excitation energy scan was later performed, with the results plotted in Figure 4.7. During the excitation energy scan, the laser output energy was increased gradually from 0 to the maximum of about 400 μJ/pulse, and the resulting LIF signal intensity was found to be following a linear relationship, and no signs of a plateau was observed. In the laser used in this study, the available energy in the 337 nm pulses is limited by the wavelength conversion setup, forcing the implementation of a high number of accumulation (1500 shots) to acquire reasonable SNR. The confirmation that the current LIF excitation energy falls in the linear regime encourages pursue of higher pulse energies. With the help of a dye laser pumped by a nanosecond Nd:YAG laser, much higher pulse energy can be acquired and single-shot 2D measurements could be possible.

4.2.3 Lifetime of Ni LIF excited at 336.96 nm

As introduced by section 2.3, it is vital that the lifetime of the LIF emission is known, so that an integrated measurement of LIF intensity can be interpreted into particle number density. In this section, measurements of the observed Ni fluorescence lines are performed.

4.2.3.1 *Camera gate delay scanning*

In a first attempt of measuring the decay lifetime of the Ni LIF emission lines, the gate of the ICMOS camera set to 2 ns was temporarily scanned against the excitation laser by varying the delay of the gate relative to the Q-switch of the laser pulses. The temporal scan was made for a total length of 4.8 ns at a step size of 0.1 ns, and the resulting spectra are stitched together as shown in Figure 4.8. The 0 ns point of the y axis was defined at the first frame in which emission from the excitation laser was observed.

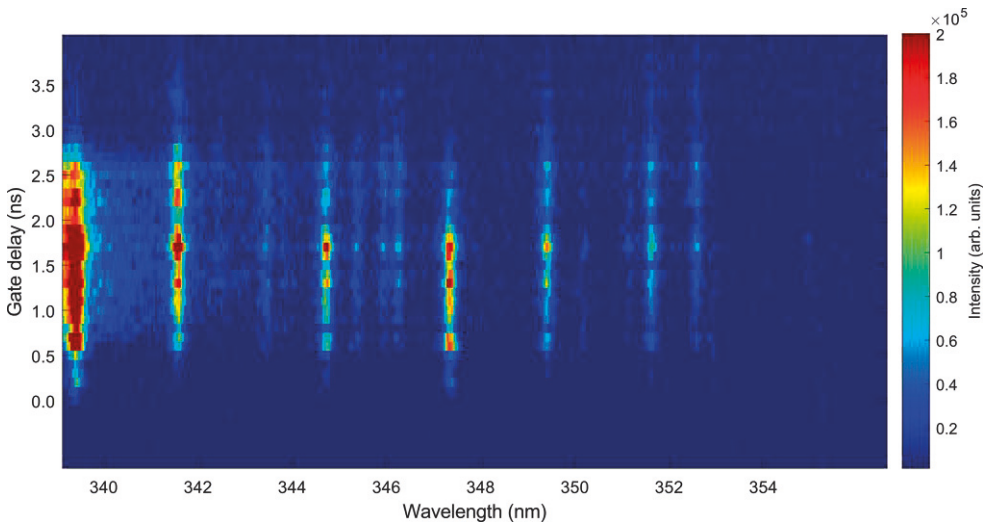

Figure 4.8: Ni LIF lifetime measurement by scanning gate delay.

From Figure 4.8, the same set of emission lines can be observed as in Figure 4.5(g), but more temporal information was revealed. The emergence of emission lines at 339.3 nm and 347.2 nm can be seen almost immediately at 0 ns delay, whereas the other lines only started to appear at least about 0.3 ns afterwards. This observation agrees with the discussions that the emission at these two wavelengths originated directly from the upper level of the excitation, while emission at other wavelengths went through a relaxation process prior to the radiative transition. Qualitatively, observations can also be made on the lifetime of individual emission lines. Among the strong emission lines, both emissions from the $3d^9(^2D)4p\ 3D_3^{\circ}$ state showed an early termination. The intensity of the two wavelengths decayed to noised level at about 3 ns. On the other hand, emission lines at 341.5 nm, 349.3 nm and 351.5

nm reached noised level at around 4 ns, exhibiting an emission duration roughly 0.5 ns longer.

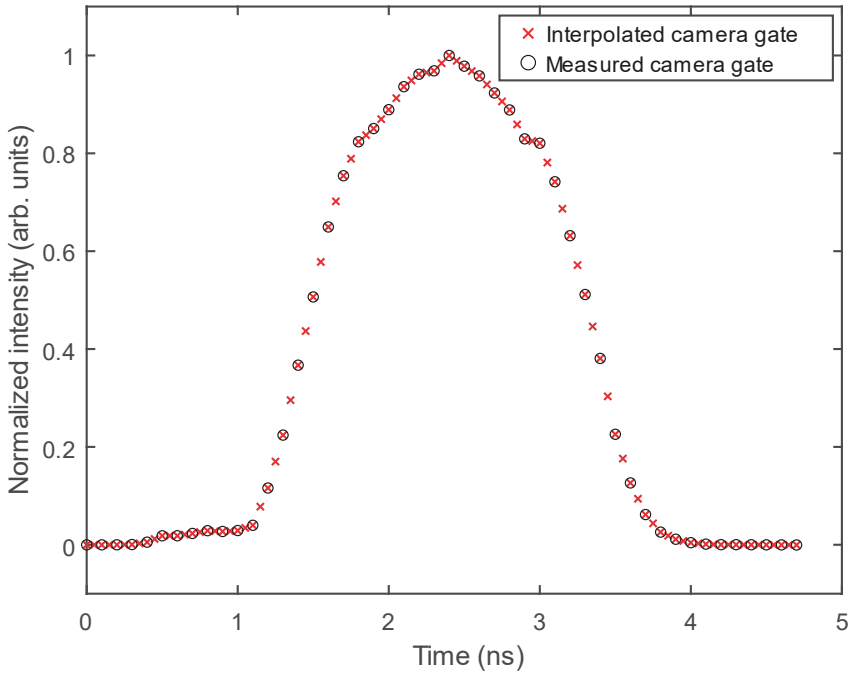

Figure 4.9: Mapped gate function of the ICMOS camera [53].

With the help of the camera gate delay scan, the gate function of the ICMOS camera was also mapped by integrating the intensity profile of the excitation laser and is depicted in Figure 4.9. As is shown in Figure 4.9, when set to a gate width of 2.1 ns, the actual gate of the ICMOS was open for about 3 ns, and the gate function is bell-shaped as opposed to being the ideal top-hat function. In contrast, the lifetimes of the observed Ni LIF transitions are no longer than 3 ns, as is illustrated in Figure 4.8. Although simulation has shown that measuring a decay with a short lifetime of about 1 ns by scanning a random gate function with a width of more than 3 ns is possible, only the data acquired at the very end of the decay can be used under such circumstances where the SNR is low and extra error may be brought into the lifetime fitting. As a result, and alternative approach was taken, that is to measure the average decay lifetime of all the transitions in the spectral range of interest with a

PMT. By using the alternative approach, spectral resolution was sacrificed, but the utilization of the PMT brought a much superior temporal response (rise time about 180 ps and fall time about 700 ps). Losing the spectral resolution was deemed acceptable since the aim of this Ni LIF study is to investigate the integrated intensity across the spectral range of interest.

4.2.3.2 PMT lifetime measurements

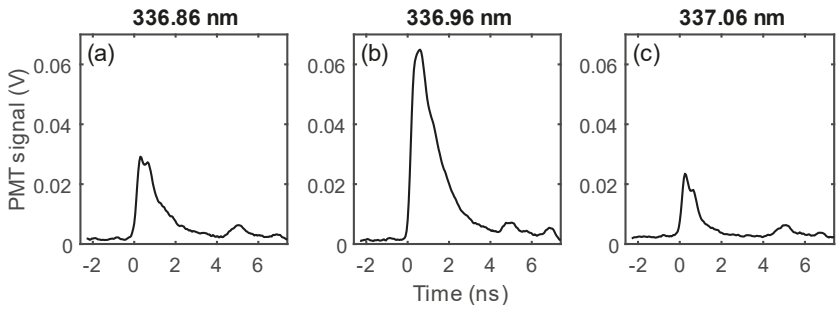

Figure 4.10: Decay curves captured with excitation wavelengths set at (a): 336.86 nm, (b): 336.96 nm and (c): 337.06 nm [53].

With the help of the PMT, decay curves were first captured at 350 μs after breakdown, at which time the highest level of spontaneous Ni atomic emission was observed in the previous study [75], when the excitation laser wavelength was set to 336.9 nm, 337.0 nm, and 337.1 nm. The resulting decay curves are shown in Figure 4.10. It can be seen from Figure 4.10 that when the laser was tuned away from the optimum excitation wavelength, a decrease in the peak signal intensity was observed, but the drop was to only about 30% of the peak intensity. To explain this phenomenon, a spectral fitting was performed to simulate the overlapping area of the Ni atomic absorption line at 336.957 nm according to literature [89, 90] and the Gaussian laser profile with a FHWM of approximately 0.1 nm. The results suggested that the laser line width was the cause of the residual intensity observed when the laser wavelength was tuned away. The simulation also showed that a -0.04 nm offset was present between the set value of the laser and the actual central wavelength. By applying the calculated offset to the laser central wavelengths, the intensity ratio between Figure 4.10 (a) and (c) was successfully reproduced. The central wavelength according to the Gaussian profile simulation was marked for each decay curve.

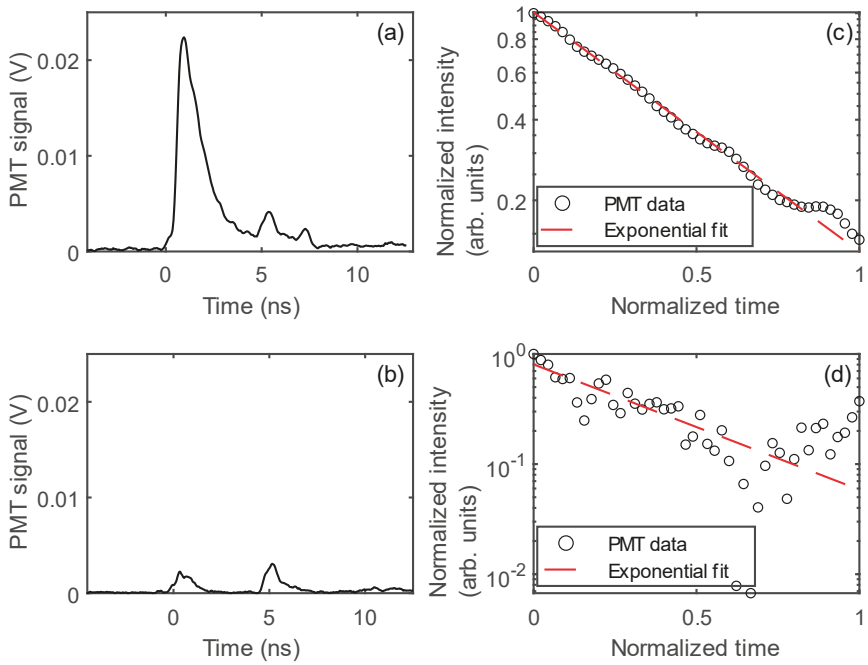

Figure 4.11: (a), (b): Captured decay curves at 150 µs and 3300 µs after breakdown; (c), (d): exponential fit of the respective decay curve [53].

In Figure 4.11, example decay curves captured by the PMT at 150 µs and 3300 µs after breakdown were shown in (a) and (b), respectively. Comparison between decay curves captured at various delays shows a common feature, the peak at about 5 ns. Across all registered decay curves, the timing of the rise as well as the intensity of the peak remained the same. Thus, we deduced that this peak was a laser-induced background, possibly originating from a random reflecting surface and that the peak should be excluded in the fitting process. Also considering that the peak of the decay should be avoided in the fitting to reduce the influence of varying peak intensity, the temporal range in which the exponential fitting was performed was determined to be between 0.65 ns and 2.90 ns. To perform the exponential fit, the intensities covered in the fitting range were normalized. The data were then shifted -0.65 ns in time and the time was also normalized for optimum fitting performance. Meanwhile, the total length of the fitting range was recorded as t_{tot}. A least-square fit was performed with MATLAB on the adjusted data using the fitting function:

$$\mathrm{f(x)} = ae^{(-\frac{x}{b})}, \qquad (4-1)$$

where a and b are fitting parameters. The lifetime of the fitted decay curve is then expressed as:

$$\tau = b * t_{tot}. \qquad (4-2)$$

With the fitting results of Figure 4.11 (a) and (b) plotted in Figure 4.11 (c) and (d), one can observe that as the LIF intensity becomes low towards the termination of the discharge. Therefore, fitting quality became much worse compared to that at the beginning of the discharge. Due to the low fitting quality, data points taken after 2300 µs after breakdown were omitted in the analysis afterwards.

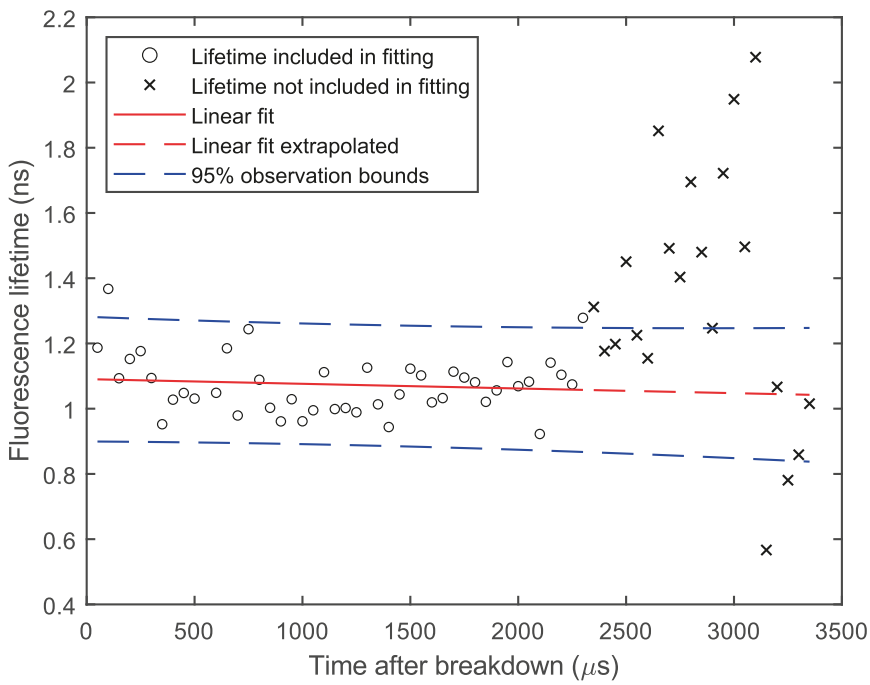

Figure 4.12: Fitted lifetime of the decays as a function of time after breakdown [53].

In Figure 4.12, fitted lifetime of the decay curves taken at different delays after breakdown were plotted, and a linear fit was performed on the lifetimes relative to time after breakdown to illustrate the trend of Ni LIF lifetime variation. Using Figure 4.12, conclusion can be drawn that with a measured deviation of about ±10%, the fluorescence lifetime of Ni atoms excited by 336.94 nm laser pulses showed no

statistically significant change across the whole duration of the spark discharge, and the average fluorescence lifetime within the spectral range of interest was about 1.1 ns.

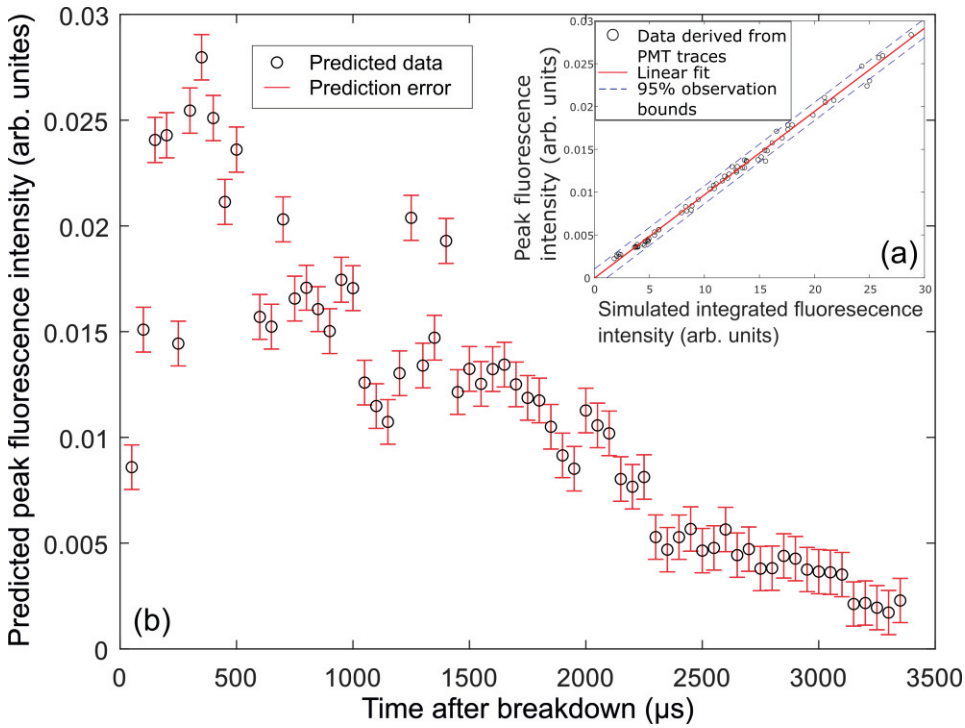

Figure 4.13: (a): Measured peak fluorescence intensity as a function of calculated integrated intensity; (b): predicted peak fluorescence intensity at various time after breakdown [53].

A convolution was performed between the gate function shown in Figure 4.9 and the captured decay curves to simulate fluorescence intensity captured by an integrating detector, and a fitting was done to examine the accuracy of predicting the peak fluorescence intensity, which is proportional to the number density of Ni atoms at ground state, using the captured fluorescence intensity, and the results are shown in Figure 4.13 (a). As can be seen, a proportional function can be used to predict the peak fluorescence intensity from measured integrated intensity, meaning that during a 2D Ni LIF measurement, the captured intensity distribution will directly reflect the Ni atom number density distribution.

Using the fitting results presented in Figure 4.13 (a), predicted peak fluorescence intensity, i.e. the Ni atom number density, was plotted against time after breakdown in Figure 4.13 (b), with the 95% prediction confidence interval plotted as the vertical red lines. Comparing Figure 4.13 (b) with the time-resolved spontaneous Ni emission profile measured in previous work [75], we can see that the predicted data based on the lifetime measurements performed in this experiment captured the trend of emission intensity variation correctly. Additionally, the prediction error is shown to be less than the data fluctuation due to other sources, such as variation in laser energy, movement of the plasma channel, difference in plasma intensity, etc. Flow field estimation

5 High-speed formaldehyde PLIF in a Research Swirler burner

The Triple Annular Research Swirler (TARS) is designed by Delavan Gas Turbine Products together with General Electric Aircraft Engines, featuring three swirling flow passages and distributed fuel injection pattern, which promotes efficient combustion with low NO_x emissions [91-94]. The intense swirls and the distributed injection pattern create strong mixing while being able to stay free from vulnerability to combustion dynamics and autoignition which are often present in pre-mixed combustors running at lean conditions [95]. While optical diagnostics have been performed to study the flow field and mixing properties of the TARS burner running on methane [91], the performance of the TARS with liquid fuel is less studied. In the current chapter, work is done performing high-speed formaldehyde LIF in a TARS combustor running on ethanol, the results of which provide some insight into the characteristics of the burner's performance when combusting a liquid fuel.

5.1 Experimental setup

5.1.1 Burner and flame conditions

Figure 5.1 illustrates the structure of the TARS burner. A cross-sectional drawing of TARS is shown in Figure 5.1 (a). In the TARS, three swirlers A (inner swirler), B (intermediate swirler), and C (outer swirler) are used for creating the three annular swirls upon the injection of air. Two fuel inlets are located on the outside of the intermediate swirler B. On the ring between swirlers B and C, eight injection holes are evenly distributed, with four facing the outer swirl and four facing the intermediate swirl.

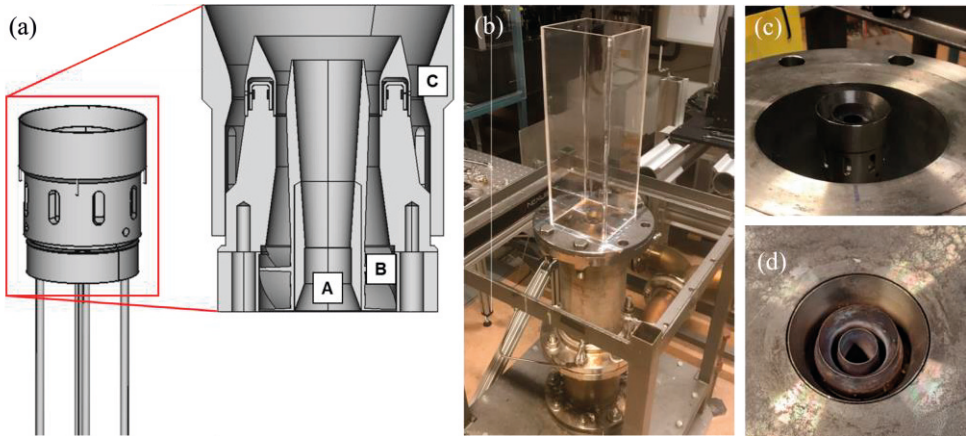

Figure 5.1: Structure of the TARS burner. (a): cross-sectional drawing of the TARS; (b): photo of the TARS burner with the quartz confinement liner; (c): photo of the TARS sitting on the burner; (d): photo of the injection port with the top plate mounted. ©Bora Orçun Çakır

An overall picture of the TARS burner is shown in Figure 5.1 (b), with detailed pictures of the TARS in Figure 5.1 (c) and (d). Air is preheated by a heater set to 280 ˚C and supplied to the burner from the bottom through an air conditioning chamber. Both fuel inlets are used for ethanol injection in order to create a more symmetrical flame structure. The flow conditions tested during the experiment are listed in Table 5-1.

Table 5-1 Flow conditions for the test cases

	Ethanol flow (ml/min)	Air flow (g/s)	Equivalence ratio	Reynolds number
Reference case	110	26	0.5	24400
Lean case	100	26	0.45	24400

5.1.2 Optical setup

The laser used in this measurement is the 355 nm pulse train generated by the THG of Quasi-modo, operated at repetition rates of 40 kHz and 50 kHz. The 355 nm pulse train was firstly expanded by a UVFS cylindrical lens (f=-100 mm) on the vertical direction, then focused using a UVFS spherical lens (f=1000 mm). The lenses were placed so that the horizontal beam waist of the 355 pulses was found at the centre of the burner's injection nozzle. The resulting laser sheet height was about 65 mm.

An average pulse energy of 130 mJ/pulse was measured at 40 kHz repetition rate, and 110 mJ/pulse at 50 kHz.

The LIF signal was filtered using two 2-inch 355 notch filters (Edmund Optics) and one GG385 long-pass filter (Schott) to prevent damage to the photocathode of the image intensifier caused by the scattered laser light. The signal was collected using a Nikkor f=50 mm *f*/1.2 imaging lens onto a high-speed camera (Photron, SA-X2) equipped with a high-speed image intensifier (LaVision, High-speed IRO).

5.2 Results and discussions

5.2.1 Formaldehyde LIF

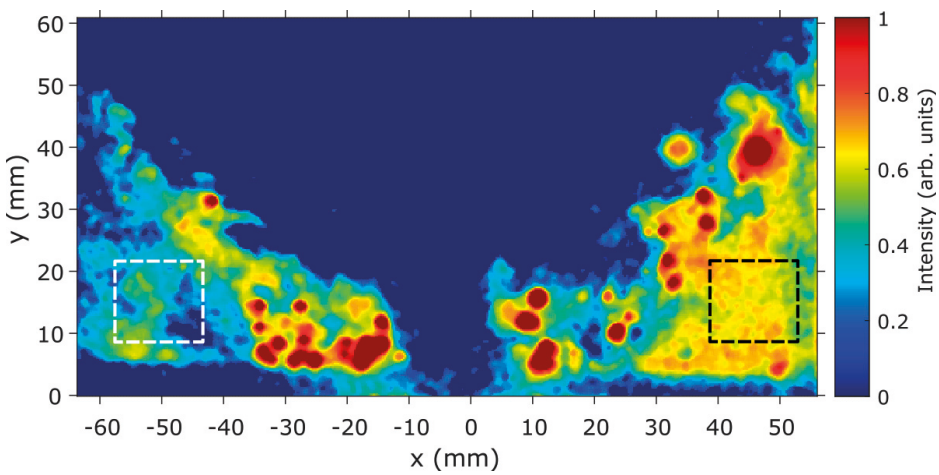

Figure 5.2: Example single shot formaldehyde PLIF image after post processing for reference case flame at repetition rate of 40 kHz, black and white dashed squares marking the regions inspected for determination of the signal thresholds.

The captured formaldehyde LIF sequences were firstly enhanced with a series of steps, including contrast stretching in the range 15%-75%, a gamma correction of 0.4, and a 5×5 median filter. An example formaldehyde PLIF image after the image enhancing steps is shown in Figure 5.2. The thresholds used for contrast stretching were determined by examining the histograms of selected regions of the acquired images, as marked by the dashed squares in Figure 5.2.

One issue revealed by Figure 5.2 is the presence of ethanol droplets. Examining across the captured frames, it is observed that formaldehyde LIF signals are found in the two triangle regions located at the bottom-right and bottom-left of the imaged region, with intensities lower than saturation. The saturated areas are the result of Mie scattered laser light, whose intensity is much higher compared to the LIF signal even after the spectral filtering. In most frames like the one shown in Figure 5.2, the droplets appear as individual saturated regions, leaving the rest of the formaldehyde signal intact. However, in certain frames, severe scattering was captured, causing imaging defects such as flare and local depletion of the photocathode, an example of which is depicted in Figure 5.3. In particular, intense flare from the droplets caused high counts of background, heavily impairing the contrast of the acquired image.

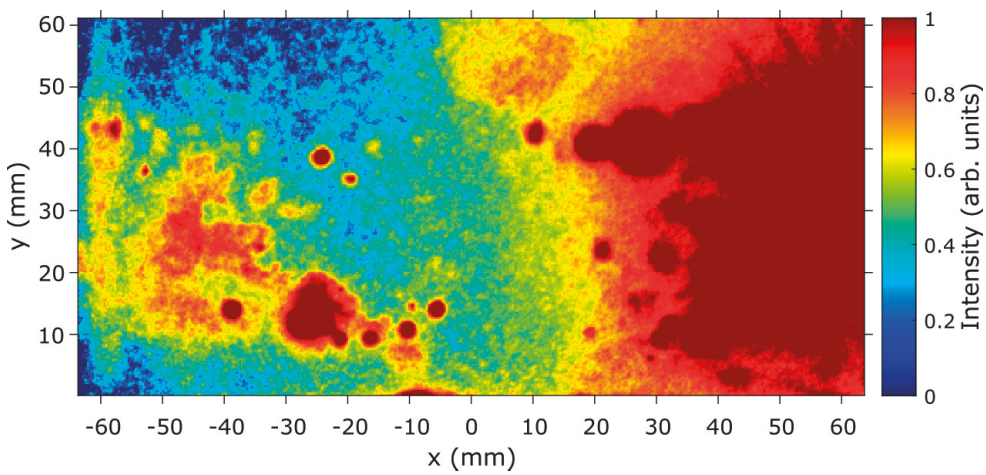

Figure 5.3: Example single shot formaldehyde PLIF image with severe interference from Mie scattering for reference case flame at 40 kHz.

Liquid ethanol is directly injected through eight distributed injection holes into the air swirls created by the three annular swirlers in the TARS. The existence of ethanol droplets is an indication of insufficient evaporation. Studying the distribution of droplets can provide information on the injection characteristics of the nozzle. As was established before, the captured formaldehyde LIF signal intensity was found to be not exceeding 75% of saturation without the influence of Mie scattered light. Following this conclusion, in the contrast stretched images, any pixel with an intensity of 1 represent occurrence of droplets. Therefore, information on droplet occurrence can be extracted from the LIF images by thresholding at 99%. Figure

5.4 shows the averaged droplet distribution in the reference case flame (a) and lean flame (b), each is an average of 160 frames acquired at 50 kHz repetition rate.

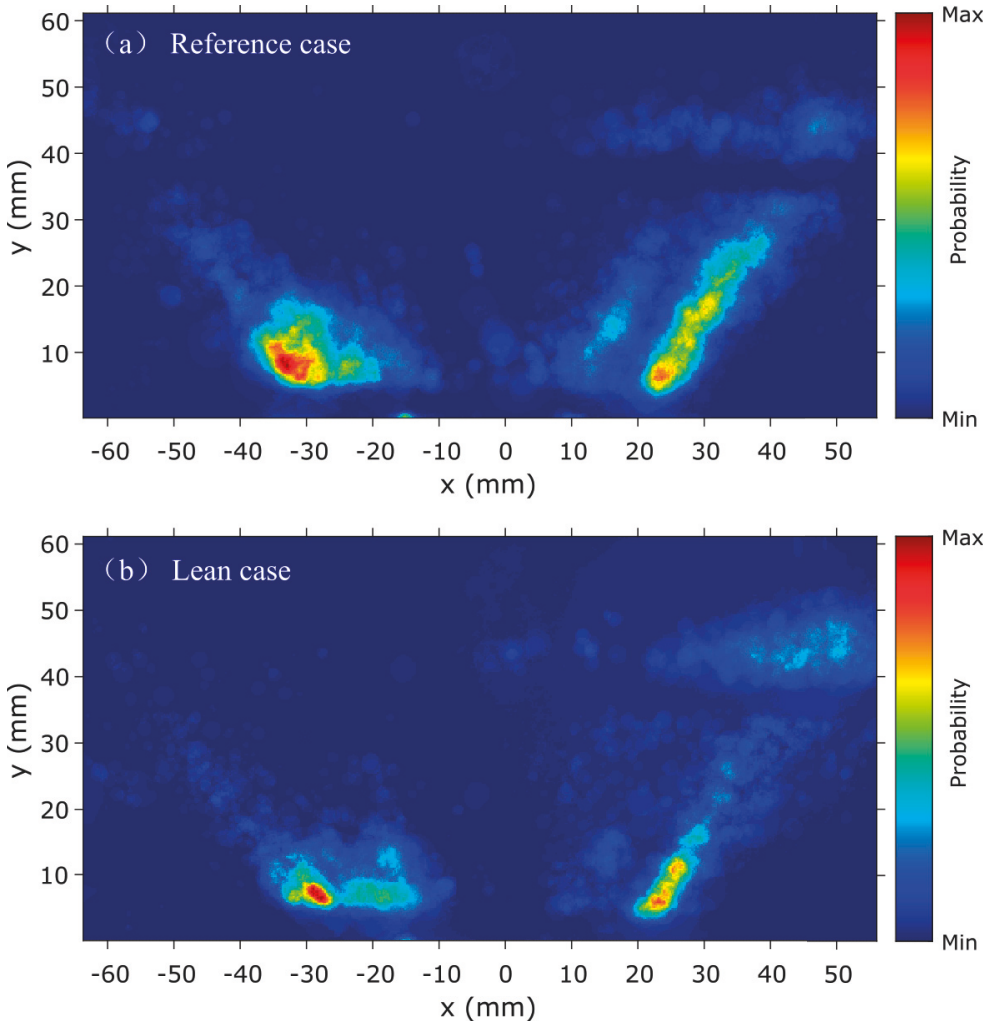

Figure 5.4: Probability map for droplet occurrence in (a): reference and (b): lean mixture cases.

Comparing the probability maps acquired at the reference case and the lean case, it can be that both cases share similar droplet distribution characteristics, where a high occurrence probability is observed close to the injection nozzle and decreases as the

vertical distance from the nozzle increases. Additionally, an asymmetry in the flame can be observed. Compared to the right side of the flame, droplets distribution is much more concentrated at lower heights on the left side of the flame. On the right side, even at a height of 40-50 mm above the burner, significant occurrence of droplets can still be seen. Comparing the reference case with the lean case, it is observed that in the lean case, droplets are found at a much smaller area. In addition, on the right side of flame, an inner layer of droplets occurrence is observed in the reference case, which cannot be seen in the lean case. Although the droplet occurrence at 20-40 mm above the burner in the lean case is consistently lower than the reference case, the probability of observing droplets at 40-50 mm above the burner is much higher for the lean case. Finally, in both cases a channel can be seen located at roughly 38 mm above the burner across the whole flame area where the droplet occurrence probability is close to zero. This is the result of the liner being damaged due to the laser running at too high pulse burst width. This is to be avoided in further measurements.

It was also found during the measurement that increase of the air preheat temperature has positive effect on reducing the number of droplets, in other words improve the evaporation. When the air preheating temperature was set to 200 ˚C, the LIF signal was overwhelmed by the Mie scattering and analysis of any kind was not possible. With the air heating temperature raised to 280 ˚C, which is the running condition for the results shown, significant reduction of droplet occurrence was achieved. Continued testing is expected in further optimizing the operating condition for a better performance.

A detailed discussion on the distribution of formaldehyde is made in the following chapter together with the estimated flow field.

5.2.2 Flow field estimation

Based on the acquired formaldehyde LIF sequences, the flow field of the measured cross section of the flame was estimated by calculating the optical flow. The optical flow calculation is carried out on the enhanced images following the procedure introduced in chapter 5.2.1. Noticing that the elastic scattering from the droplets can introduce signal interference, causing vectors to appear where no formaldehyde signal is detected, a region of interest has been manually selected and applied to all images before the optical flow calculations.

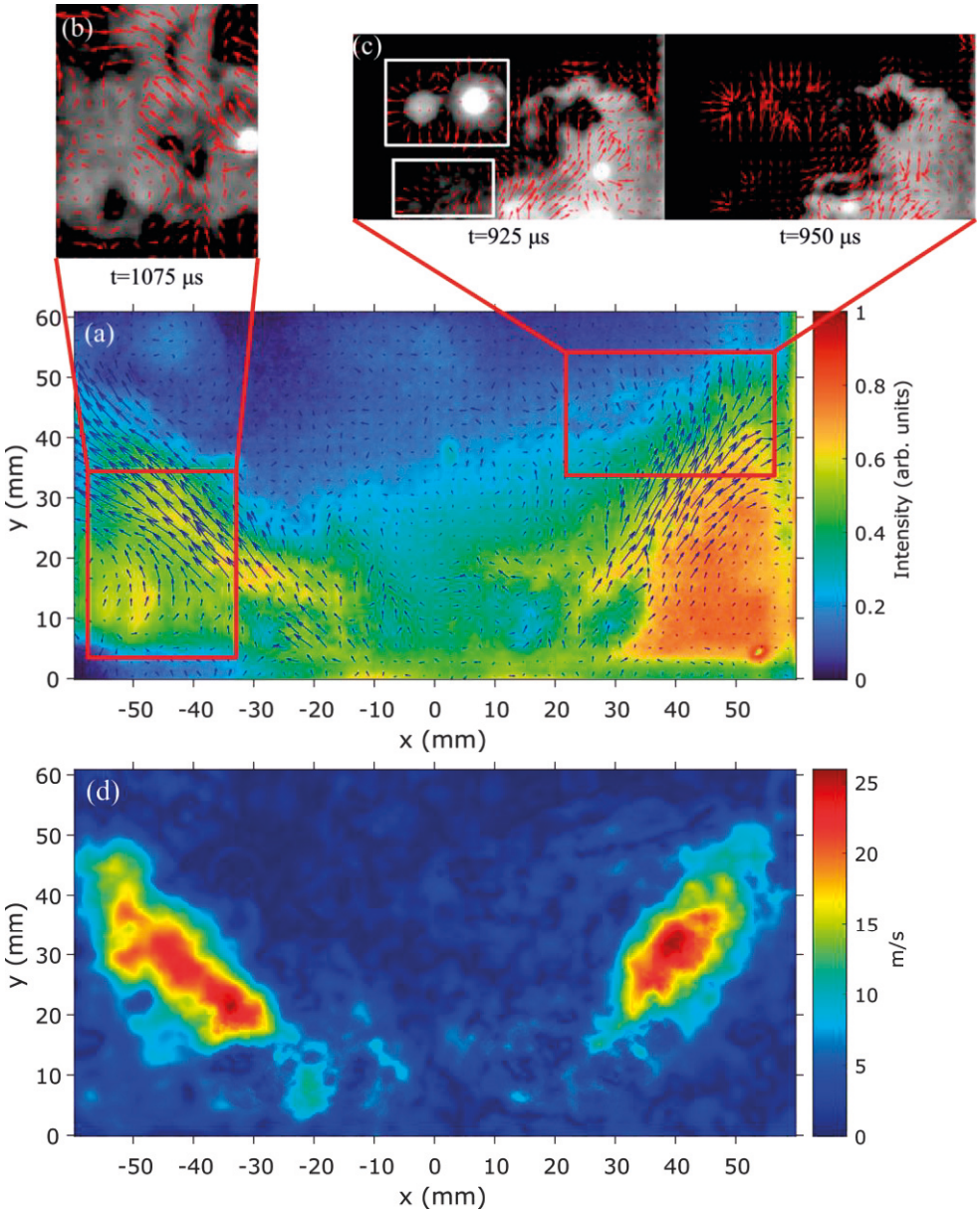

Figure 5.5 (a): Averaged flow field derived from optical flow of formaldehyde LIF plotted over the averaged distribution of formaldehyde; (b): single-shot formaldehyde LIF with flow field illustrating the recirculation zone; (c): zoomed-in images showing occurrence and disappearance of droplets disrupting the optical flow calculation; (d): the magnitude plot of the averaged flow field.

The optical flow algorithm used was the Farneback method provided by MATLAB. In this method, a pyramid decomposition is used to generate an image pyramid, consisting of multiple levels that have lower resolution at a higher level, and tracking of motion gets refined as the algorithm proceeds into higher levels [96]. Compared with the other methods provided in MATLAB, the Farneback method was shown to behave more robustly against the interference of saturated points created by the Mie scattering of ethanol droplets. While performing the optical flow calculations, a pyramid level of 3 was used with a scaling factor of 0.1. A Gaussian filter size of 28 was set for the averaging of the calculated flow field, which helps improving the algorithm's robustness against image noise as well as the Mie scattering.

Figure 5.5 shows the mean flow field derived from the 40 kHz formaldehyde LIF sequence on the reference case flame, plotted over the averaged formaldehyde distribution. The algorithm was shown to succeed in capturing the flow characteristics from the high-speed formaldehyde LIF sequence, as is illustrated in Figure 5.5 (b). From Figure 5.4 it is found out that the region selected for Figure 5.5 (b) is less affected by droplets, and the algorithm could capture the outer recirculation zone with good precision. Even local small scale flow structure can be characterized.

However, the presence of Mie scattering from the droplets complicates the situation. While performing the optical flow estimation, one must take into consideration that the occurrence and disappearance of droplets breaks the assumption of optical flow that the total intensity of the same area before and after movement remains the same, thus causing disruptions to the calculated flow field, an example of which is depicted in Figure 5.5 (c). Similar effect could also be created due to the out-of-plane motion in the swirls. Therefore, to make use of the single-shot flow field data, care has to be taken to make sure that the inspected frames are free of droplet influence. However, as shown in Figure 5.5 (c), in the frames where sudden appearance of a droplet is observed, the optical flow algorithm results in vectors pointing out of the centre of the droplet, while in the consecutive frame where the same droplet disappears, vectors point at the centre were calculated. This means that by averaging the field, the influence of individual droplets can be reduced, thus ensuring that the averaged optical flow result is a good representative of the actual flow field. The magnitude of the averaged flow field is illustrated in Figure 5.5 (d).

Combining Figure 5.5 (a) and (d), it is found out that the TARS demonstrated insufficient droplet breakup and evaporation at the current operating condition, which in turn caused insufficient mixing. Previously acquired formaldehyde PLIF results in similar burner designs with well mixed mixtures usually show a formaldehyde distribution as a slightly thickened layer in the pre-heat zone, with a little excess formaldehyde present in the outer recirculation zone at suboptimal conditions [97-99]. In comparison, it is observed that under the current operating condition, high amount of formaldehyde is found to be trapped in the outer

recirculation zone. This trapping of formaldehyde could be the result of serval reasons. For example, possibility could be that part of the fuel directly enters the outer recirculation zone without contributing to the flame front.

To follow up on the discussion, further investigation with fuel tracer PLIF could reveal the fuel distribution upon injection, and together with the acquired formaldehyde PLIF better describe the characteristics of the TARS burner. Optimization of the operating conditions is possible with the help of the two diagnostic approaches.

6 Quasi-simultaneous high-speed tomographic LIF of dual species

While traditional planar imaging techniques have been very successful at revealing spatially resolved details of combustion processes, combustion involved in most applications have a 3D nature, which cannot be accurately captured by conventional 2D methods. For example, in gas turbine flames, PLIF can capture distribution of species at a cross section of the flame with high precision [97, 100], but in the gas turbine flame there exists a swirl motion that enhances mixing and plays an important role in stabilizing the flame [101], which is not observed in the 2D slices. Such flames are also highly turbulent, and turbulent flows have 3D structures and motions by nature [102], necessitating the advance to the 3D measurement space.

As is discussed in chapter 2.4, the application of computed tomography in LIF in flames faces a challenge of being highly hardware demanding. In this chapter, an alternative approach is described, which is capable of performing a quasi-simultaneous acquisition of 3D LIF of two species, anisole as a fuel tracer and formaldehyde, using two high-speed CMOSs and intensifiers.

6.1 Experimental setup

6.1.1 The 4-splitting imaging optics

Shown in Figure 6.1 is a schematic drawing of the 4-splitting imaging setup. To aid the description, a local coordinate system is established, where the x axis is same direction as the camera, and the z axis points up in the vertical direction, as is marked in Figure 6.1. The 4-splitting setup splits the imaging sensor to a 2 by 2 matrix. M1-4 are two-inch UV enhanced aluminium mirrors used for signal collection. On the top level of the sensor matrix, signal collected by M3 and M4 are reflected into the B.Halle f=100 *f*/2 UV lens by a pair of 25 mm size UVFS right angle prisms. Prisms are used here instead of mirrors because the reflecting surfaces must be placed as close as possible to gain the most optimum signal intensity after the reflection. On the bottom level, a customized holder was used to hold two one-inch UV enhanced aluminium mirrors to reflect the signals collected by M1 and M2.

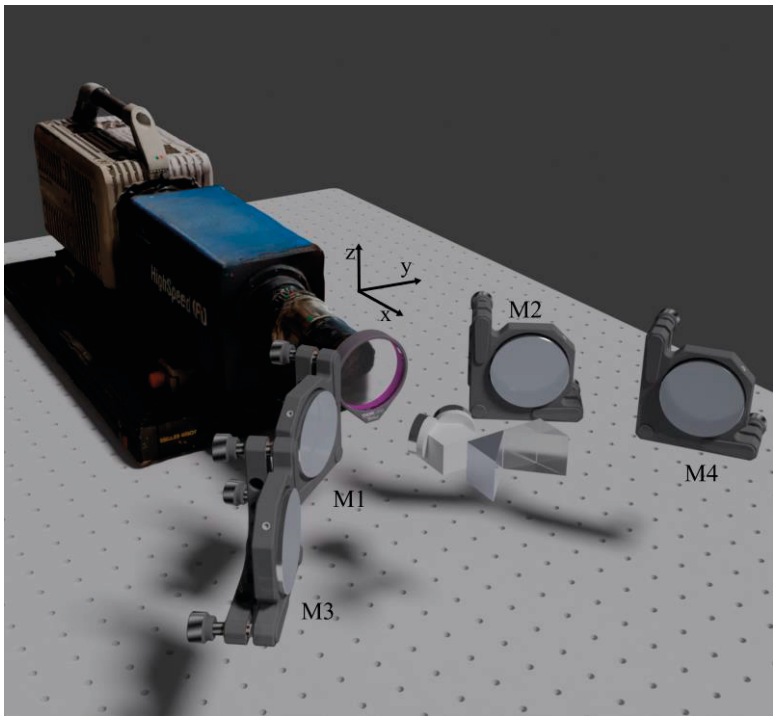

Figure 6.1: Schematic drawing of one channel with the 4-splitting imaging setup.

For all four mirrors to be placed on the same height along z axis, M1 and M2 must be tilted down. The purpose of the customized holder is to tilt the two one-inch mirrors up to compensate for the down tilting of M1 and M2, while keeping the distance between the two reflecting surfaces at a minimum. A too large distance will result in severe signal loss when the images are centred on the imaging sensor. The positions of M1 and M2 can be adjusted. The y axis positions decide the angle coverage of the system, and the x axis positions can be adjusted to compensate for the difference in optical path length of the two levels, making sure that a sharp focus can be achieved in all four split views.

In the actual measurement, two channels of the system described in Figure 6.1 were used. Due to limit of accessible devices, the two channels were equipped with different cameras and intensifiers. In one channel, a Photron Fastcam SA-X2 was used together with a Lavison High-speed IRO image intensifier. In the other channel, a Photron Fastcam SA-Z was used with a Lambert HiCATT image intensifier. The

sensor resolution must be kept identical on both channels and was limited by the Photron Fastcam SA-X2 to 768×768.

6.1.2 Laser setup

In order to achieve a quasi-simultaneous imaging of two species on the same sensor, the doublet mode of the Quasi-modo was used in this experiment. The laser was set to run at 10 kHz repetition rate, and the output wavelengths of 266 nm and 355 nm were used as the excitation source for anisole and formaldehyde, respectively. The 355 nm pulse train was passed through a double pass delay line with 3 m length. In such way, a doublet containing two pairs of 266 nm and 355 nm pulses were created, with the separation between the two pairs of pulses being 5 μs and within each pulse pair the 355 nm pulse being delayed by 20 ns compared to the 266 nm pulse. A detailed discussion on the setting of the delay can be found in chapter 6.2.

After the 6 m delay line, the 355 nm pulse train suffered from increased beam divergence over the horizontal direction, therefore different beam shaping optics were required for the two wavelengths. A pair of cylindrical lenses were used to expand the 355 nm pulse train on the vertical direction (f_1=-1000 mm, f_2=300 mm, UVFS). For the 266 nm pulse train, a telescope consisting of two spherical UVFS lenses (f_1=-75 mm, f_2=125 mm) was used to expand the beam. The resulting cross section sizes were approximately 9 mm (horizontal) × 10 mm (vertical) for the 355 nm pulse train, and 9 × 9 mm for the 266 nm pulse train. A 266 nm high reflector with 45˚ AOI was used to join the two pulse trains together.

Two stages of flash lamp amplifiers were turned on during the measurement. After optimizing the phase matching angles of the THG and FHG units, temperature of the SHG crystal was carefully adjusted to balance the intensity of the anisole LIF and formaldehyde LIF. In the measurement, a crystal temperature of 150.1˚ was used, delivering an average doublet energy of about 150 mJ at 355 nm and 26 mJ at 266 nm. Considering that the intensity ration between the two pulses in the doublet was about 2:1 and the first pulse of the pair was used for excitation of formaldehyde while the second for anisole, about 100 mJ/pulse was used to excite formaldehyde, and roughly 8.7 mJ/pulse for anisole excitation.

6.1.3 Burner configuration

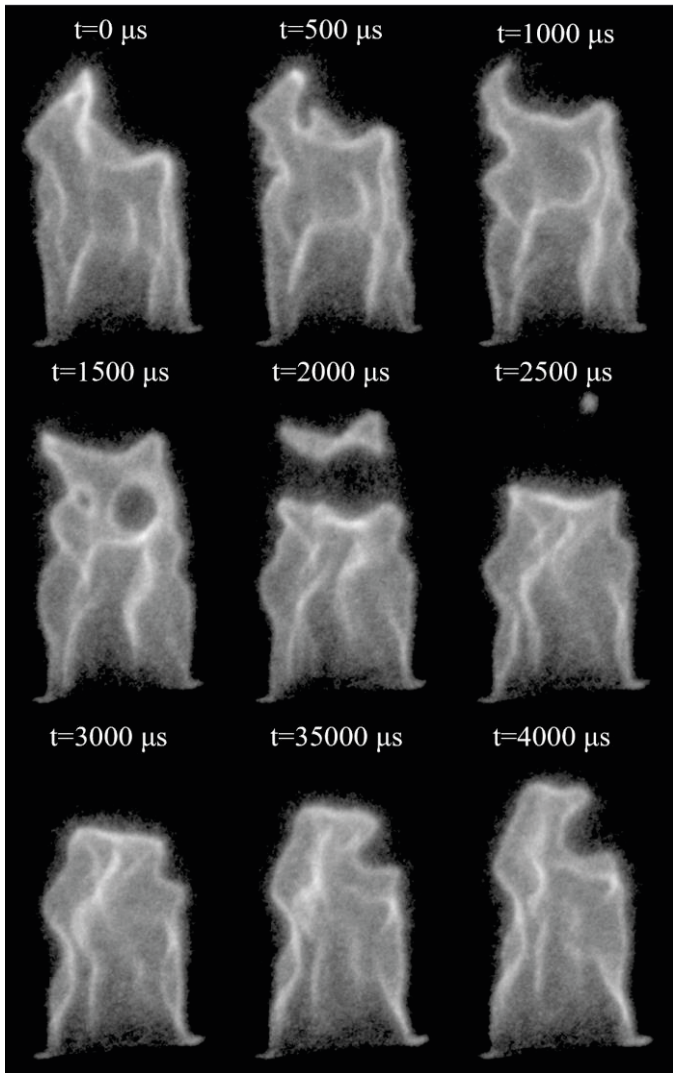

Figure 6.2: Chemiluminescence sequence of the propane flame used in the experiment.

The burner used in this experiment was a Bunsen burner. With the air inlet of the burner closed, the flame condition was fully controlled by a pair of Bronkhorst mass flow controllers. Before mixing with the propane in a pre-mixing tube about 1 m long, the air supplied to the burner was bubbled through a bottle of anisole at room temperature, resulting in a seeding concentration of approximately 0.41% [103]. The flows used in the measurement case was 3.00 L/min air and 0.45 L/min propane, forming a pre-mixed flame with an equivalence ration of about 3.57. With a 9.3 mm

inner diameter of the burner, the Reynolds number of the pre-mixed flow was estimated to be about 642. As is shown in Figure 6.2, despite the relatively low Reynolds number, the flame demonstrated characteristics of turbulent combustion, such as the wrinkling of the flamelets. In the shown image sequence, it has also been observed that a breaking of the reaction surface has happened between t=1000 µs and t=3000 µs, suggested by the chemiluminescence at the top of the flame detaching from the bulk region and slowly consumed.

6.2 Timing design for quasi-simultaneous LIF of dual species

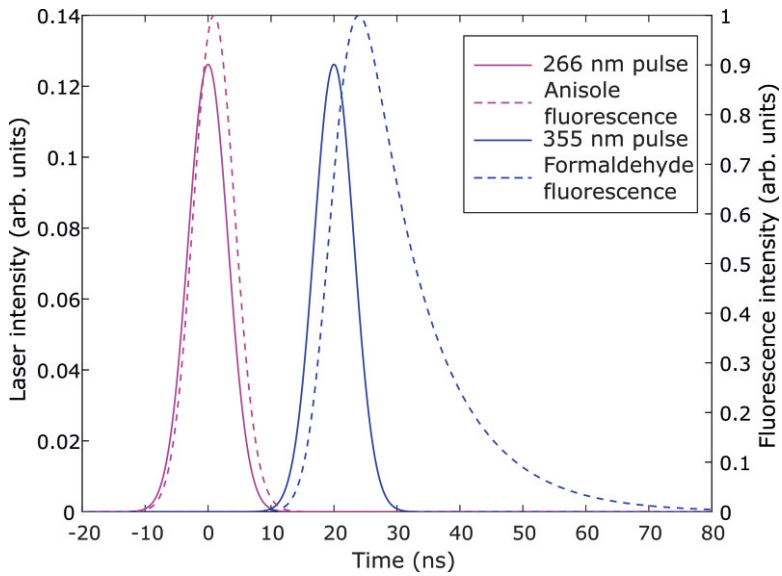

Figure 6.3: Schematic drawing of the temporal profiles of the excitation pulses and the fluorescence signals.

The fluorescence lifetimes of anisole and formaldehyde must be taken into consideration when designing the timing of the pulses. According to previous research, a fluorescence lifetime of approximately 1 ns is expected for anisole excited at 266 ns in atmospheric flame conditions [24] and 10 ns for formaldehyde [104]. Tests have shown that propagating the pulse train generated by the Quasi-modo at prolonged distances can lead to severe degradation of beam quality, and

the pulse train will suffer from increased beam divergence. Given the restriction of beam quality as well as the spacing in the lab, a double pass delay line over a distance of 3 m was the maximum that could be used, resulting in a temporal delay between the 266 nm pulse and the 355 nm pulse of about 20 ns. The pulses in the pulse train have a FWHM of approximately 10 ns.

The temporal profiles of the excitation pulses and the corresponding fluorescence signals are shown in Figure 6.3. Since the figure is aimed for demonstration of the temporal characteristics, the peak intensity of the pulses was assumed to be the same, and the fluorescence traces of anisole and formaldehyde were normalized against their peak values.

As can be seen in Figure 6.3, a 10 ns lifetime of formaldehyde LIF means that the formaldehyde fluorescence signal is more than 20% the peak value 20 ns after the peak excitation intensity is reached. This suggests that the separation of fluorescence signals in time is insufficient, should the 266 nm pulse train be sent through the delay line. As a result, the 355 nm pulse train is sent through the delay line in the current experiment, and the high-speed cameras register formaldehyde fluorescence with the first pair of pulses in the doublet, and anisole using the second pair.

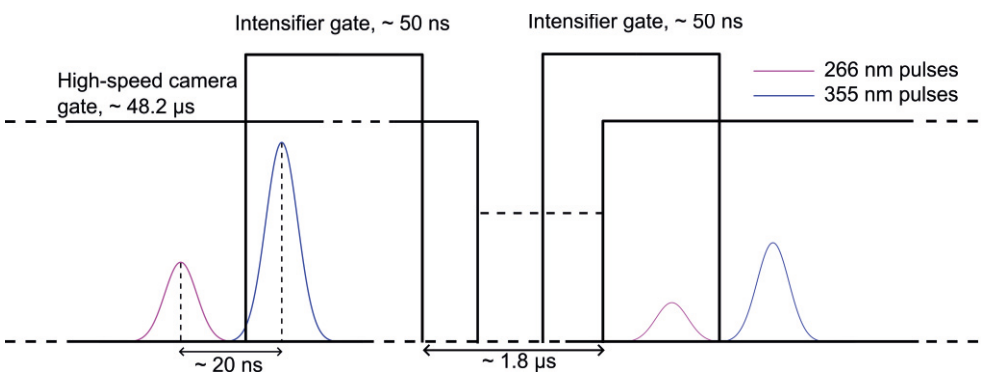

Figure 6.4: Schematic drawing of the synchronization among high-speed camera, image intensifier and the laser pulses.

The synchronization setup used in the experiment is illustrated in Figure 6.4. In the experiment prior to data collection, the gate timing of the intensifier must be scanned with only one wavelength allowed through the flame. The delay was carefully adjusted to make sure that signal crosstalk between the adjacent frames does not exceed noise level. It is also worth noting that the ratio of energy for the two pulse

pairs in the doublet is about 2:1 with the first pair of pulses being stronger than the second pair, as was described in chapter 6.1.2. During the experiment, it has been observed that anisole fluorescence signal is much stronger compared to formaldehyde, despite the excitation energy of anisole being less than 20% of formaldehyde. The current synchronization scheme captures formaldehyde LIF with the strong pulse pair and anisole with the weak pair, therefore aiding the balancing of intensity for the two species.

6.3 Spatial calibration of the imaging system

An accurate calibration of all the viewing angles is essential for a successful reconstruction. In this section, a detailed description of the calibration process and some discussions are presented.

In the current experiment, a 9 × 10 checkerboard pattern consisting of 2 × 2 mm squares was used as the target. The target was printed and glued to a flat piece of metal plate to ensure minimum distortion and was illuminated with a flashlight during the calibration process.

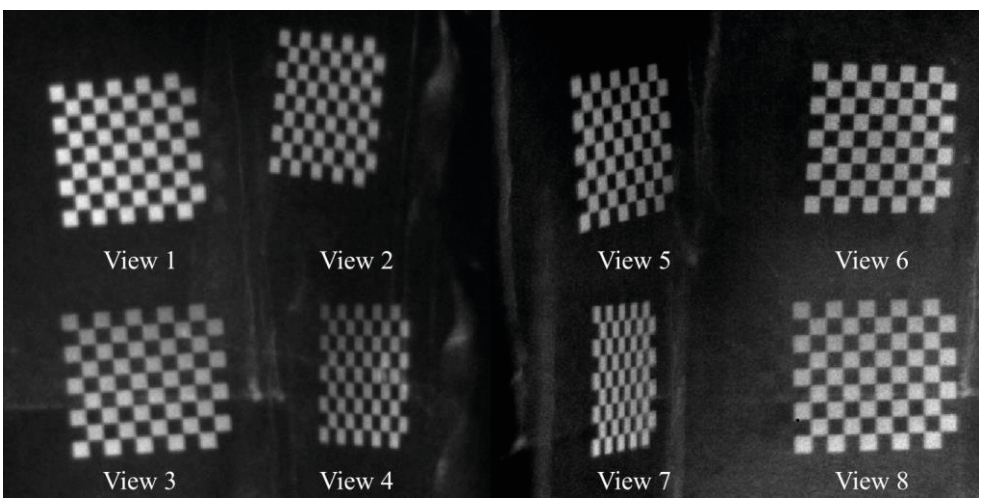

Figure 6.5: Example frame during spatial calibration.

The first frame of the calibration was captured with the target put at a position where the pattern is visible from all the eight viewing angles. This step is of high

importance to a successful calibration, as the spatial calibration for each view is carried out individually and this frame is used to stitch all views together. After capturing the reference frame, the target was rotated at small step sizes around its yaw axis and images were taken after each rotation. At various yaw angles, the pitch and roll of the target was also changed. In total, about 100 frames were registered for the whole calibration process. The calibration was carried out both prior to the measurement and after the measurement. An example frame used for calibration is shown in Figure 6.5.

After data collection, the raw images were segmented and the segments from the same view were grouped together. The calibration is performed using the Camera Calibrator app from MATLAB with each viewing angle treated as an individual camera. The extrinsics of each camera (viewing angle) were estimated based on a pinhole camera model. Due to the fact that the imaging lens has a relatively long focal length of 100 mm, and that only the centre of the imaging area was used, a low degree of image distortion was expected, therefore no distortion correction was used during the calibration. After acquiring the spatial information for each view individually, all eight views are joint together in the same space with the aid of the first captured frame.

The nature of the sensor splitting strategy leads to the fact that cross talk exists between adjacent viewing angles if a homogenous illumination over the whole imaged area is applied. Therefore, measure must be taken to avoid edges of adjacent views intruding into the checkerboard area of the current view. During the current measurement, the checkerboard pattern was printed with a black background, and the edges of the metal board to which the target was glued were covered with black paper. Such measures did reduce the signal cross talk, but some influence is still visible. In particular, views 3 and 8 can be seen to have impaired contrast, as is shown in Figure 6.5. It should be noted that the signal cross talk is only a problem during calibration, as the volume that is fluorescing during measurement is well defined and does not extend beyond the imaged area of the corresponding view.

Another factor that could hurt the accuracy of the calibration is the fact that the target was printed on paper and illuminated externally. In such a setup, the contrast between the white squares and the black ones of the checkerboard pattern is not optimum. Additionally, at certain pitch angles, the printed target reflects the illuminated light into the detector, making the contrast even worse. Ideally one should use an active source as the calibration target. The calibration benefits from the enhanced contrast and the cross talk can be avoided.

After spatial calibration, an intensity calibration was also performed to account for the difference in collection efficiency among the views. In this step, a white sheet of paper illuminated from the back side was placed at the detection volume, and the images were taken on both imaging channels. The intensity ratio among the views

were found out, and corrections were made accordingly to the measured data afterwards.

7 Phosphor thermometry on injection nozzle surface of a lab-scale gas turbine burner

7.1 Experimental setup

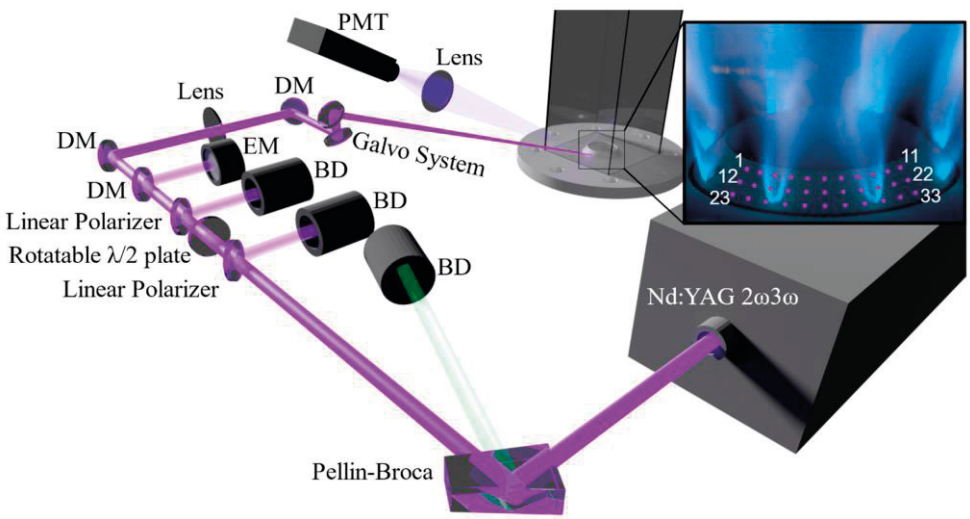

Figure 7.1: Experimental setup for surface thermometry on the injection nozzle of a lab-scale burner. EM: energy meter; DM: dichroic mirror; BD: beam dump. The zoomed in view illustrates measured points on the injection nozzle surface [105].

The experimental setup for the surface thermometry measurement on the injection nozzle of a lab-scale gas turbine burner is shown in Figure 7.1. The excitation laser used was the third harmonic of an Nd:YAG laser at 10 Hz. The energy of the excitation laser was controlled by rotating a half-wave plate placed between two linear polarizers whose polarization was perpendicular to each other. About 16 µJ

of pulse energy was focused to a spot with a diameter of about 1.5 mm, resulting in a laser fluence of 0.9 mJ/cm^2. The phosphor used in this experiment was ZnS:Ag, whose emission was filtered by a band-pass filter centred at 450 nm with a 40 nm FWHM, a 355 nm notch filter, and a 385 nm long-pass filter before passing into a Hamamatsu H11526-20-NF PMT.

In this experiment, the laser focal point was navigated on the surface of the injection nozzle using a galvo system, which is an assembly of two mirrors each motorized around an axis. A program drove the motors so that a detection matrix of 11×3 points cover about 90˚ of the nozzle at three different heights. The detection matrix is illustrated in Figure 7.1 in the zoomed in view. At each measurement point, 50 decay curves were accumulated and the lifetime of the accumulated decay curves were fitted using a trust-region-reflective least-squares fitting algorithm in MATLAB with the model equation:

$$I(t) = I_0 \exp\left(-\frac{t}{\tau}\right) + I_{offset}, \qquad (7-1)$$

where τ is the lifetime. The measured lifetimes were interpreted as temperature with the help of a calibration curve of the phosphor acquired using similar methodology as described in [106].

In the experiment, three different nozzles, featuring pilot flames that are diffusive (DP1), low degree partially premixed (PP2), and high degree partially premixed (PP3), respectively, were tested with two kinds of fuels, pure methane and 50% hydrogen-enriched methane. Detailed pilot injection strategies can be found in [105].

7.2 Results

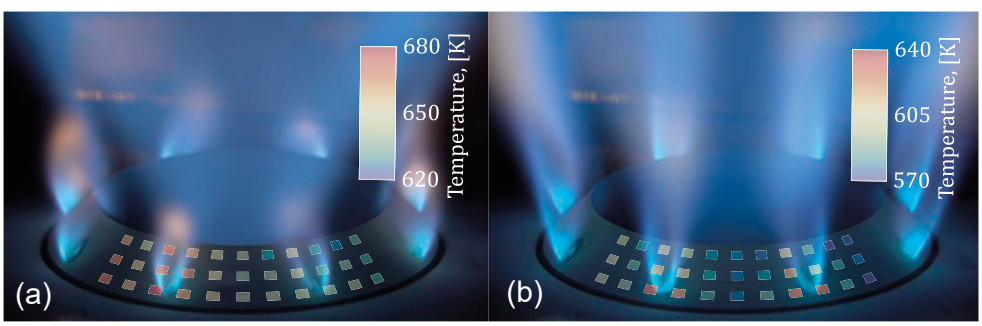

Figure 7.2: Integrated chemiluminescence of flame and measured surface temperature. Injection nozzle: DP1; 1% air and 6% fuel used as pilot; fuel used: (a): CH_4, (b): H_2/CH_4 [105].

In Figure 7.2, the measured surface temperature matrices for the DP1 nozzle run with 1% air flow and 6% fuel flow as the pilot are overlayed on photos of the flame chemiluminescence and the nozzle. Figure 7.2 (a) and (b) show the results for pure methane and hydrogen-enriched methane, respectively. An overall comparison between Figure 7.2 (a) and (b) illustrates that the temperature profile is about 20 K higher using pure CH_4 as the fuel compared to using hydrogen-enriched methane. The same conclusion holds true across all combinations of injection nozzle type and pilot flow percentage. The overall difference in injection nozzle temperature is the result of the reduced thermal power in the hydrogen-enriched methane flame due to the limitation of flame stability. Equivalence ratios of Φ=0.72 and Φ=0.52 were selected for pure methane and hydrogen-enriched methane, respectively, for the two flames to end up approximately at the same position in the stability map presented in [100]. The cooling effect of the pilot flow is depicted by Figure 7.2 in the uneven temperature profile. From the right of the measuring matrix to the left, an increasing trend can be observed, which can be explained by the cold pilot air and fuel flow entering the nozzle plate from the right side and feeding the injection holes shown in Figure 7.2 from right to left. Such a flow scheme led to the cold air and fuel flow taking more heat from the right side of the measurement matrix, contributing to the uneven temperature profile. The cooling effect was observed to be dominant by the air flow in the pilot, as the flow rate of air is much higher than that of the fuel, when air is present in the pilot.

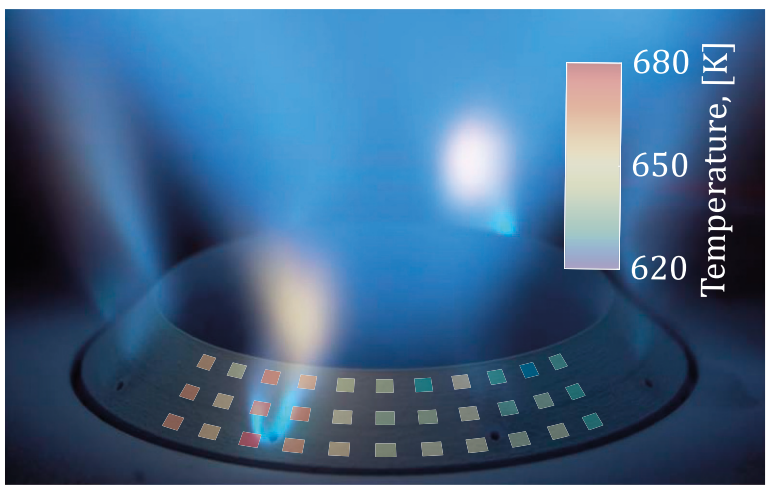

Figure 7.3: Integrated chemiluminescence of flame and measured surface temperature. Injection nozzle: DP1; 2% air and 2% fuel used as pilot; pure methane [105].

Local heating introduced by the pilot flame attaching to the nozzle surface was captured by the scanning of the galvo system. In both Figure 7.2 and 7.3, local temperature rise can be observed at points around the nozzle holes. In Figure 7.3, a case is shown where pilot flame attachment was evident on the left hole, but no visible flame can be observed on the right hole. This absence of the pilot flame attachment on the right was consistent throughout the measurements, the reason of which could arise from either the irregularity during the 3D printing process, or the routing of the fuel lines causing a difference in the fuel flow. As can be seen, a temperature increase of about 30 K was measured at the points next to the left hole, whereas the temperature profile was almost constant around the right hole. This further emphasised the importance of local heating by pilot flame attachment.

8 Conclusions and outlook

In this thesis, optical diagnostics have been developed in multiple applications centred around energy conversion processes. The construction of an injection-seeded OPO for high-speed burst mode operation has achieved a partial success. A stable cavity has been constructed and a routine for building and aligning of the cavity has been established. For the first time, LIF was used in studying the electrode erosion characteristics during spark plug discharges. Detailed study on the fluorescence properties of Ni atoms has been performed and foundation has been laid for further studies. An improved sensor splitting strategy for carrying out tomography measurement has been demonstrated, together with a tailored triggering scheme that allowed quasi-simultaneous acquisition of two species on a single sensor. In the TARS burner, high-speed formaldehyde PLIF confirmed the existence of high amount of ethanol droplets and revealed an insufficiency in fuel-air mixing, emphasizing the importance of improvement by optimizing the TARS configuration and burner running conditions.

The OPO is currently faced with a problem of unsuccessful sum frequency generation. Measures are to be taken in the future to improve the beam quality of the 609 nm pulses output from the OPO, and further attempts should be made to acquire 284 nm pulses at a stable energy level, granting us the ability to perform OH LIF. With access to OH information, more systematic information can be gained over multiple combustion applications. For example, OH PLIF will reveal the reacted region in the TARS burner flame, providing insight into the structure of the inner recirculation zone, which also plays an important role in the stabilization of the flame.

With known information on the fluorescence lifetime of Ni atoms in the spark plug gap, possibility of PLIF study on the Ni atom distribution and generation characteristics is unlocked. Various ignition parameters of the spark plug, such as breakdown voltage, ignition coil energy, ambient pressure and ambient gas composition, will be tested to study how they can affect t the erosion of the electrode. Quasi-modo could also be a powerful tool. With its high repetition rate, one can even perform temporally resolved diagnostic within a single discharge. Such measurements can be highly interesting for revealing the dynamics during the decaying discharge plasma.

In the TARS burner, the results from formaldehyde LIF puts emphasis on taking measures to improve mixing. On the diagnostic side, additional fuel tracer PLIF can be helpful in showing the mixing conditions. With the help of both techniques, systematic study on burner parameters affecting the mixing can be performed. Moreover, with the access to 284 nm pulses, simultaneous multi-species diagnostic on the flame can be possible, illustrating the full picture of TARS ethanol combustion.

The improved sensor splitting strategy for tomography reconstruction succeed in restraining all views approximately on the same horizontal plane. This is very helpful in application where the optical access is limited, such as in an optical engine. Continued work can also be put in further refining the design, achieving a better signal collection efficiency and more even distribution of signal amongst the views. The timing strategy has been proven to be able to temporally separate LIF signals from two species with an optical setup with minimum complexity. Application of such strategy can easily be generalized to other combinations of other species.

Lifetime based phosphor thermometry measurement has been performed on three different models of injection nozzles in a lab-scale gas turbine burner. The use of a galvo system ensured automation and repeatability of the measurement over a 3×11 matrix of target points on the nozzles' surface. The results revealed that the nozzle's surface temperature was primarily dependent on global heating from the main flame, cool effect by the supplied fuel and air, and local heating from attached pilot flames.

9 References

1. Ahmad, T. and D. Zhang, *A critical review of comparative global historical energy consumption and future demand: The story told so far.* Energy Reports, 2020. **6**: p. 1973-1991.
2. Kalghatgi, G., *Is it the end of combustion and engine combustion research? Should it be?* Transportation Engineering, 2022. **10**: p. 100142.
3. IEA, *World Energy Outlook 2022*, IEA, Editor. 2022: Paris.
4. IEA, *Net Zero by 2050*. 2021, IEA: Paris.
5. Leplat, N., et al., *Numerical and experimental study of ethanol combustion and oxidation in laminar premixed flames and in jet-stirred reactor.* Combustion and Flame, 2011. **158**(4): p. 705-725.
6. Olm, C., et al., *Development of an Ethanol Combustion Mechanism Based on a Hierarchical Optimization Approach.* International Journal of Chemical Kinetics, 2016. **48**(8): p. 423-441.
7. Petrova, M.V. and F.A. Williams, *A small detailed chemical-kinetic mechanism for hydrocarbon combustion.* Combustion and Flame, 2006. **144**(3): p. 526-544.
8. Zettervall, N., C. Fureby, and E.J.K. Nilsson *Evaluation of Chemical Kinetic Mechanisms for Methane Combustion: A Review from a CFD Perspective*. Fuels, 2021. **2**, 210-240 DOI: 10.3390/fuels2020013.
9. Aldén, M., *Spatially and temporally resolved laser/optical diagnostics of combustion processes: From fundamentals to practical applications.* Proceedings of the Combustion Institute, 2023. **39**(1): p. 1185-1228.
10. Slipchenko, M.N., et al., *All-diode-pumped quasi-continuous burst-mode laser for extended high-speed planar imaging.* Optics Express, 2013. **21**(1): p. 681-689.
11. Slipchenko, M.N., et al., *Quasi-continuous burst-mode laser for high-speed planar imaging.* Optics Letters, 2012. **37**(8): p. 1346-1348.
12. Jiang, N., M.C. Webster, and W.R. Lempert, *Advances in generation of high-repetition-rate burst mode laser output.* Applied Optics, 2009. **48**(4): p. B23-B31.
13. Thurow, B., et al., *Narrow-linewidth megahertz-rate pulse-burst laser for high-speed flow diagnostics.* Applied Optics, 2004. **43**(26): p. 5064-5073.
14. Miles, P.P.W.R.B., *High-energy pulse-burst laser system for megahertz-rate flow visualization.* Optics Letters, 2000. **25**(22): p. 3.
15. Eckbreth, A.C., *Laser-induced fluoresecence(LIF)*, in *Laser diagnostics for combustion temperature and species*. 1996, Overseas Publishers Assosiation Amsterdam B.V.: Netherlands. p. 381-466.

16. Daily, J.W., *Laser induced fluorescence spectroscopy in flames.* Progress in Energy and Combustion Science, 1997. **23**(2): p. 133-199.
17. Mbayachi, V.B., et al., *Laser-Induced Fluorescence in Combustion Research*, in *Advanced Diagnostics in Combustion Science*, Z.-Y. Tian, Editor. 2023, Springer Nature Singapore: Singapore. p. 223-243.
18. Aldén, M., et al., *Visualization and understanding of combustion processes using spatially and temporally resolved laser diagnostic techniques.* Proceedings of the Combustion Institute, 2011. **33**(1): p. 69-97.
19. Kohse-Höinghaus, K., et al., *Combustion at the focus: laser diagnostics and control.* Proceedings of the Combustion Institute, 2005. **30**(1): p. 89-123.
20. Co, D.T., et al., *Rotationally Resolved Absorption Cross Sections of Formaldehyde in the 28100−28500 cm-1 (351−356 nm) Spectral Region: Implications for in Situ LIF Measurements.* The Journal of Physical Chemistry A, 2005. **109**(47): p. 10675-10682.
21. Tran, K.H., et al., *Fluorescence spectroscopy of anisole at elevated temperatures and pressures.* Applied Physics B, 2014. **115**(4): p. 461-470.
22. Harrington, J.E. and K.C. Smyth, *Laser-induced fluorescence measurements of formaldehyde in a methane/air diffusion flame.* Chemical Physics Letters, 1993. **202**(3): p. 196-202.
23. Kiefer, J., et al., *OH-thermometry using laser polarization spectroscopy and laser-induced fluorescence spectroscopy in the OH A-X (1,0) band.* Journal of Raman Spectroscopy, 2009. **40**(7): p. 828-835.
24. Faust, S., T. Dreier, and C. Schulz, *Photo-physical properties of anisole: temperature, pressure, and bath gas composition dependence of fluorescence spectra and lifetimes.* Applied Physics B, 2013. **112**(2): p. 203-213.
25. Jeunehomme, M. and A.B.F. Duncan, *Lifetime Measurements of Some Excited States of Nitrogen, Nitric Oxide, and Formaldehyde.* The Journal of Chemical Physics, 1964. **41**(6): p. 1692-1699.
26. Yamasaki, Y. and A. Tezaki, *Non-linear pressure dependence of A-state fluorescence lifetime of formaldehyde.* Applied Physics B, 2005. **80**(7): p. 791-795.
27. Wang, Z., et al., *Transition from HCCI to PPC: Investigation of Fuel Distribution by Planar Laser Induced Fluorescence (PLIF).* SAE International Journal of Engines, 2017. **10**(4): p. 1465-1481.
28. Wang, Z., et al., *Ultra-high-speed PLIF imaging for simultaneous visualization of multiple species in turbulent flames.* Opt Express, 2017. **25**(24): p. 30214-30228.
29. Wang, Z., et al., *Simultaneous 36 kHz PLIF/chemiluminescence imaging of fuel, CH2O and combustion in a PPC engine.* Proceedings of the Combustion Institute, 2019. **37**(4): p. 4751-4758.
30. Wang, Z., et al., *Structure and burning velocity of turbulent premixed methane/air jet flames in thin-reaction zone and distributed reaction zone*

regimes. Proceedings of the Combustion Institute, 2019. **37**(2): p. 2537-2544.
31. Gomez, M., et al., *Four-dimensional laser-induced fluorescence and tomography of liquids.* International Journal of Multiphase Flow, 2023. **166**.
32. Halls, B.R., et al., *20-kHz-rate three-dimensional tomographic imaging of the concentration field in a turbulent jet.* Proceedings of the Combustion Institute, 2017. **36**(3): p. 4611-4618.
33. Halls, B.R., et al., *kHz-rate four-dimensional fluorescence tomography using an ultraviolet-tunable narrowband burst-mode optical parametric oscillator.* Optica, 2017. **4**(8).
34. Halls, B.R., et al., *Single-shot, volumetrically illuminated, three-dimensional, tomographic laser-induced-fluorescence imaging in a gaseous free jet.* Opt Express, 2016. **24**(9): p. 10040-9.
35. Roy, S., et al., *4D imaging of fast flow dynamics: From challenging dream to reality*, in *8th Bsme International Conference on Thermal Engineering*. 2019.
36. Bahaa E. A. Saleh, M.C.T., *Nonlinear Optics*, in *Fundamentals of Photonics*. 1991, John Wiley & Sons Inc. p. 873-935.
37. Franken, P.A., et al., *Generation of Optical Harmonics.* Physical Review Letters, 1961. **7**(4): p. 118-119.
38. Akbari, R. and A. Major, *Optical, spectral and phase-matching properties of BIBO, BBO and LBO crystals for optical parametric oscillation in the visible and near-infrared wavelength ranges.* Laser Physics, 2013. **23**(3).
39. Chen, C., et al., *New nonlinear-optical crystal: LiB3O5.* Journal of the Optical Society of America B, 1989. **6**(4): p. 616-621.
40. Chen, C.-T. and G.-Z. Liu. *Recent advances in nonlinear optical and electro-optical materials*. in *IN: Annual review of materials science. Volume 16 (A87-23168 08-23). Palo Alto*. 1986.
41. Hulme, K.F., *Nonlinear optical crystals and their applications.* Reports on Progress in Physics, 1973. **36**(5): p. 497.
42. CHEN, C., et al., *A NEW-TYPE ULTRAVIOLET SHG CRYSTAL——β-BaB_2O_4.* Science in China Series B-Chemistry, Biological, Agricultural, Medical & Earth Sciences, 1985. **28**(3): p. 235-243.
43. Ganeev, R.A., et al., *Characterization of nonlinear optical parameters of KDP, $LiNbO_3$ and BBO crystals.* Optics Communications, 2004. **229**(1): p. 403-412.
44. Nikogosyan, D.N., *Beta barium borate (BBO), A review of its properties and applications.* Applied Physics A, 1991. **52**(6): p. 359-368.
45. Smith, A.V., D.J. Armstrong, and W.J. Alford, *Increased acceptance bandwidths in optical frequency conversion by use of multiple walk-off-compensating nonlinear crystals.* Journal of the Optical Society of America B, 1998. **15**(1): p. 122-141.
46. Hu, X.P., P. Xu, and S.N. Zhu, *Engineered quasi-phase-matching for laser techniques [Invited].* Photonics Research, 2013. **1**(4): p. 171-185.

47. Myers, L.E. and W.R. Bosenberg, *Periodically poled lithium niobate and quasi-phase-matched optical parametric oscillators.* IEEE Journal of Quantum Electronics, 1997. **33**(10): p. 1663-1672.
48. Zhu, S.-n., Y.-y. Zhu, and N.-b. Ming, *Quasi-Phase-Matched Third-Harmonic Generation in a Quasi-Periodic Optical Superlattice.* Science, 1997. **278**(5339): p. 843-846.
49. Lakowicz, J.R., *Quenching of Fluorescence*, in *Principles of Fluorescence Spectroscopy*, J.R. Lakowicz, Editor. 1983, Springer US: Boston, MA. p. 257-301.
50. Aldén, M., et al., *Thermographic phosphors for thermometry: A survey of combustion applications.* Progress in Energy and Combustion Science, 2011. **37**(4): p. 422-461.
51. Allison, S.W., *A brief history of phosphor thermometry.* Measurement Science and Technology, 2019. **30**(7).
52. Khalid, A.H. and K. Kontis, *Thermographic Phosphors for High Temperature Measurements: Principles, Current State of the Art and Recent Applications.* Sensors, 2008. **8**(9): p. 5673-5744.
53. Ruike Bi, K.Z., Andreas Ehn, Mattias Richter, *Lifetime of Ni laser induced fluorescence during spark plug discharge* Applied Physics B, 2024. **130**(147).
54. Miller, V.A., V.A. Troutman, and R.K. Hanson, *Near-kHz 3D tracer-based LIF imaging of a co-flow jet using toluene.* Measurement Science and Technology, 2014. **25**(7): p. 075403.
55. Nygren, J., et al., *Three-dimensional laser induced fluorescence of fuel distributions in an HCCI engine.* Proceedings of the Combustion Institute, 2002. **29**(1): p. 679-685.
56. Wellander, R., M. Richter, and M. Aldén, *Time-resolved (kHz) 3D imaging of OH PLIF in a flame.* Experiments in Fluids, 2014. **55**(6): p. 1764.
57. Dong, R., et al., *Analysis of Global and Local Hydrodynamic Instabilities on a High-Speed Jet Diffusion Flame via Time-Resolved 3D Measurements.* Flow, Turbulence and Combustion, 2021. **107**(3): p. 759-780.
58. Kang, M., X. Li, and L. Ma, *Three-dimensional flame measurements using fiber-based endoscopes.* Proceedings of the Combustion Institute, 2015. **35**(3): p. 3821-3828.
59. Liu, H., B. Sun, and W. Cai, *kHz-rate volumetric flame imaging using a single camera.* Optics Communications, 2019. **437**: p. 33-43.
60. Floyd, J., P. Geipel, and A.M. Kempf, *Computed Tomography of Chemiluminescence (CTC): Instantaneous 3D measurements and Phantom studies of a turbulent opposed jet flame.* Combustion and Flame, 2011. **158**(2): p. 376-391.
61. Grauer, S.J., et al., *Volumetric emission tomography for combustion processes.* Progress in Energy and Combustion Science, 2023. **94**: p. 101024.

62. Grauer, S.J., et al., *Instantaneous 3D flame imaging by background-oriented schlieren tomography.* Combustion and Flame, 2018. **196**: p. 284-299.
63. Halls, B.R., et al., *4D spatiotemporal evolution of combustion intermediates in turbulent flames using burst-mode volumetric laser-induced fluorescence.* Opt Lett, 2017. **42**(14): p. 2830-2833.
64. Meyer, T.R., et al., *High-speed, three-dimensional tomographic laser-induced incandescence imaging of soot volume fraction in turbulent flames.* Opt Express, 2016. **24**(26): p. 29547-29555.
65. Pareja, J., et al., *A study of the spatial and temporal evolution of auto-ignition kernels using time-resolved tomographic OH-LIF.* Proceedings of the Combustion Institute, 2019. **37**(2): p. 1321-1328.
66. Li, T., et al., *Tomographic imaging of OH laser-induced fluorescence in laminar and turbulent jet flames.* Measurement Science and Technology, 2018. **29**(1).
67. Ma, L., et al., *Direct comparison of two-dimensional and three-dimensional laser-induced fluorescence measurements on highly turbulent flames.* Optics Letters, 2017. **42**(2): p. 267-270.
68. Sanned, D., et al., *Arbitrary position 3D tomography for practical application in combustion diagnostics.* Measurement Science and Technology, 2022. **33**(12).
69. Hult, J., et al., *Application of a high-repetition-rate laser diagnostic system for single-cycle-resolved imaging in internal combustion engines.* Applied Optics, 2002. **41**(24): p. 5002-5014.
70. Pan, R., et al., *Generation of high-energy, kilohertz-rate narrowband tunable ultraviolet pulses using a burst-mode dye laser system.* Optics Letters, 2018. **43**(5): p. 1191-1194.
71. Maly, R., *Spark Ignition: Its Physics and Effect on the Internal Combustion Engine*, in *Fuel Economy: in Road Vehicles Powered by Spark Ignition Engines*, J.C. Hilliard and G.S. Springer, Editors. 1984, Springer US: Boston, MA. p. 91-148.
72. Craver, R.J., R.S. Podiak, and R.D. Miller, *Spark plug design factors and their effect on engine performance.* SAE Transactions, 1970: p. 229-239.
73. Lin, H.T., et al., *Characterization of erosion and failure processes of spark plugs after field service in natural gas engines.* Wear, 2005. **259**(7-12): p. 1063-1067.
74. Kailun Zhang, R.B., Johan Tidholm, Jakob Ängeby, Mattias Richter, Andreas Ehn (unpublished), *Detection of Nickel Atoms Released from Electrodes in Spark Discharges Using Laser-induced Fluorescence.*
75. Bi, R., *Time-Resolved Diagnostic of Electrode Erosion in Spark Plugs*. 2019, Lund University: Lund, Sweden.
76. Astanei, D., et al. *Optical emission spectroscopy diagnostic of air-plasma produced by a double spark-plug*. in *XXXIIth International Conference on Phenomena in Ionized Gases (ICPIG)*. 2015.

77. Hnatiuc, B., et al., *Diagnostic of Plasma Produced by a Spark Plug at Atmospheric Pressure: Reduced Electric Field and Vibrational Temperature.* Contributions to Plasma Physics, 2014. **54**(8): p. 712-723.
78. Kim, W., et al. *Spatio-temporally resolved emission spectroscopy of inductive spark ignition in atmospheric air condition*. in *Ignition systems for gasoline engines: 4th international conference*. 2018.
79. Oliveira, C., et al., *Optical and electrical diagnostics of a spark-plug discharge in air.* Journal of Physics D: Applied Physics, 2012. **45**(25): p. 255201.
80. Kim, Y.-C., et al., *Correlation between vibrational temperature of N2 and plasma parameters in inductively coupled Ar/N2 plasmas.* Physics of Plasmas, 2015. **22**(8).
81. Rehman, N.U., et al., *Metrology of non-thermal capacitively coupled N2–Ar mixture plasma.* Optics Communications, 2013. **296**: p. 72-78.
82. Xiao, D., et al., *Characteristics of atmospheric-pressure non-thermal N2 and N2/O2 gas mixture plasma jet.* Journal of Applied Physics, 2014. **115**(3).
83. Coulombe, S. and J.-L. Meunier, *Importance of high local cathode spot pressure on the attachment of thermal arcs on cold cathodes.* IEEE transactions on plasma science, 1997. **25**(5): p. 913-918.
84. Coulombe, S. and J.-L. Meunier, *Theoretical prediction of non-thermionic arc cathode erosion rate including both vaporization and melting of the surface.* Plasma Sources Science and Technology, 2000. **9**(3): p. 239.
85. Kramida, A., Ralchenko, Yu., Reader, J., and NIST ASD Team *NIST Atomic Spectra Database (ver. 5.11)*, in *Online*. 2023, National Institute of Standards and Technology, Gaithersburg, MD.: Available: https://physics.nist.gov/asd
86. Lawler, M.E.W.J.E., *Atomic Transition Probabilities in Ni I.* The Astrophysical Journal Supplement Series, 1997. **110**(1): p. 3.
87. Blackwell, D., et al., *Measurement of relative oscillator strengths for Ni I. Transitions from levels a^3F_{4-2}(0.00-0.27 eV), a^3D_{3-1}(0.03-0.21 eV) and a^1D_2(0.42 eV).* Monthly Notices of the Royal Astronomical Society, 1989. **236**(2): p. 235-245.
88. Wysong, I.J., J.B. Jeffries, and D.R. Crosley, *Laser-induced fluorescence of O(3p^{3}P), O_2, and NO near 226 nm: photolytic interferences and simultaneous excitation in flames.* Optics Letters, 1989. **14**(15): p. 767-769.
89. Doerr, A. and M. Kock, *Ni I oscillator strengths.* Journal of Quantitative Spectroscopy and Radiative Transfer, 1985. **33**(4): p. 307-318.
90. Huber, M. and R. Sandeman, *Oscillator strengths of ultraviolet NI I lines from hook-method and absorption measurements in a furnace.* Astronomy and Astrophysics, 1980. **86**: p. 95-104.
91. Iudiciani, P., et al. *Characterization of a Multi-Swirler Fuel Injector Using Simultaneous Laser Based Planar Measurements of Reaction Zone,*

Flow Field, and Fuel Distribution. in *ASME Turbo Expo 2009: Power for Land, Sea, and Air*. 2009.
92. Li, G. and E.J. Gutmark. *Experimental and Numerical Studies of the Velocity Field of a Triple Annular Swirler*. in *ASME Turbo Expo 2002: Power for Land, Sea, and Air*. 2002.
93. Li, G. and E.J. Gutmark. *Geometry Effects on the Flow Field and the Spectral Characteristics of a Triple Annular Swirler*. in *ASME Turbo Expo 2003, collocated with the 2003 International Joint Power Generation Conference*. 2003.
94. Li, G. and E.J. Gutmark, *Effect of exhaust nozzle geometry on combustor flow field and combustion characteristics.* Proceedings of the Combustion Institute, 2005. **30**(2): p. 2893-2901.
95. Li, G. and E.J. Gutmark. *Effects of Swirler Configurations on Flow Structures and Combustion Characteristics*. in *ASME Turbo Expo 2004: Power for Land, Sea, and Air*. 2004.
96. Farnebäck, G. *Two-Frame Motion Estimation Based on Polynomial Expansion*. in *Image Analysis*. 2003. Berlin, Heidelberg: Springer Berlin Heidelberg.
97. Subash, A.A., et al., *Flame investigations of a laboratory-scale CECOST swirl burner at atmospheric pressure conditions.* Fuel, 2020. **279**: p. 118421.
98. Allison, P.M., et al., *Coupling of flame geometry and combustion instabilities based on kilohertz formaldehyde PLIF measurements.* Proceedings of the Combustion Institute, 2015. **35**(3): p. 3255-3262.
99. Böckle, S., et al., *Simultaneous single-shot laser-based imaging of formaldehyde, OH, and temperature in turbulent flames.* Proceedings of the Combustion Institute, 2000. **28**(1): p. 279-286.
100. Pignatelli, F., et al., *Pilot impact on turbulent premixed methane/air and hydrogen-enriched methane/air flames in a laboratory-scale gas turbine model combustor.* International Journal of Hydrogen Energy, 2022. **47**(60): p. 25404-25417.
101. Huang, Y. and V. Yang, *Dynamics and stability of lean-premixed swirl-stabilized combustion.* Progress in Energy and Combustion Science, 2009. **35**(4): p. 293-364.
102. Masri, A.R., *Challenges for turbulent combustion.* Proceedings of the Combustion Institute, 2021. **38**(1): p. 121-155.
103. *National Center for Biotechnology Information (2024), PubChem Compound Summary for CID 7519, Anisole.* Retrieved February 22, 2024 from https://pubchem.ncbi.nlm.nih.gov/compound/Anisole.
104. Tobai, J. and T. Dreier, *Effective A-state fluorescence lifetime of formaldehyde in atmospheric pressure CH4/air flames.* Applied Physics B, 2002. **74**(1): p. 101-104.
105. Feuk, H., et al. *Impact of Methane and Hydrogen-Enriched Methane Pilot Injection on the Surface Temperature of a Scaled-Down Burner Nozzle Measured Using Phosphor Thermometry*. International Journal of

Turbomachinery, Propulsion and Power, 2022. **7**, DOI: 10.3390/ijtpp7040029.
106. Nada, F.A., et al., *Development of an automatic routine for calibration of thermographic phosphors.* Measurement Science and Technology, 2014. **25**(2): p. 025201.

Summary of papers

Paper I

Detection of Nickel Atoms Released from Electrodes in Spark Discharges using Laser-induced Fluorescence

Kailun Zhang, **Ruike Bi**, Johan Tidholm, Jakob Ängby, Mattias Richter, Andreas Ehn

In this paper, we did an excitation scan on Ni atoms generated by a spark discharge and studied the emission spectrum of Ni under different excitation wavelengths. We found an optimum excitation wavelength of 336.9 nm yielding the highest signal within a detection window between 341 and 351 nm.

Kailun and I designed the experiment and performed the measurements together. Kailun did most of the data analysis while I provided support. Kailun wrote the manuscript.

Paper II

Lifetime of Ni Laser Induced Fluorescence During Spark Plug Discharge

Ruike Bi, Kailun Zhang, Andreas Ehn, Mattias Richter

In this paper, the fluorescence lifetime of Ni atoms present in a spark plug discharge excited by 336.9 nm laser pulses was studied. A linear correlation was made between the number density of Ni atoms and the detected LIF intensity using the measured lifetime. Using the conclusion above, generation of Ni atoms by a DC inductive discharge was studied, showing that Ni number density reaches maximum early during the discharge, and keeps decreasing as the discharge continues.

Kailun and I designed the experiment and performed the measurements together. I did the data analysis. I created the figures and wrote the manuscript.

Paper III

Quasi-simultaneous, High-speed Tomographic Fluorescence Imaging of Fuel Tracer and Formaldehyde in a Propane Flame

Ruike Bi, David Sanned, Panagiota Stamatoglou, Mattias Richter

In this paper, improvements were made to an existing strategy to split camera views in order to achieve 3D tomographic reconstruction using only 2 cameras. A novel triggering scheme allowed quasi-simultaneous acquisition of tomographic LIF of two species using no additional cameras. The proposed strategy was demonstrated on a turbulent propane flame, acquiring 3D distribution of fuel tracer and formaldehyde at 10 kHz repetition rate in a turbulent propane flame.

I initiated this study. I designed and 3D-printed the designated holder used in the data collection setup. Panagiota and I prepared the laser and set up the optical arrangements. David and I performed calibration of the tomography reconstruction, and I conducted the flame measurements. David did the 3D reconstructions. I wrote the manuscript except the technical section about tomographic reconstruction, which was written by David.

Paper IV

Impact of Methane and Hydrogen-Enriched Methane Pilot Injection on the Surface Temperature of a Scaled-Down Burner Nozzle Measured Using Phosphor Thermometry

Henrik Feuk, Francesco Pignatelli, Arman Subash, **Ruike Bi**, Robert Zoltán Szász, Xue Song Bai, Daniel Lörstad, Mattias Richter

A galvo system was used to perform phosphor thermometry measurement on a matrix of points on injection nozzles of a lab-scale gas turbine burner, yielding 2D temperature information. The surface temperatures of the nozzle under different fuels, injection nozzle types, and fuel injection strategies were investigated. OH PLIF and flame chemiluminescence data were also taken to associate the flame condition to local heating of the nozzle.

Henrik and I built the optical setup for phosphor thermometry and performed the thermometry measurements. I took the chemiluminescence images of the flame. Henrik, Francesco, Arman, and I contributed to the interpretation of the measurement results. Henrik and Francesco wrote the manuscript.